REGIONAL BODY-WAVE TOMOGRAPHY OF THE PERUVIAN FLAT SLAB

Bissett E. Young

A thesis submitted to the faculty of the University of North Carolina at Chapel Hill in partial fulfillment of the requirements for the degree of Master of Science in the Department of Geological Sciences.

Chapel Hill
2014

Approved by:

Lara Wagner

Gordana Vlahovic

Kevin Stewart

ABSTRACT

Bissett E. Young: Regional body-wave tomography of the Peruvian flat slab
(Under the direction of Lara Wagner)

Local travel time data were used to create three dimensional tomography models of V_p and V_s above the flat slab in southern Peru, where the Nazca plate subducts subhorizontally beneath the continental lithosphere. The Peruvian flat slab segment corresponds to a gap in the volcanic arc and far-field thick-skinned deformation in the Eastern Cordillera. Despite ongoing research, there is little consensus on the causes and consequences of flat slab subduction. We present results from regional body-wave tomography which show high S-wave velocities above the slab for a region that coincides with the location of the Nazca ridge, a bathymetric high subducting at $\sim 15°$S. We propose that fast S-wave arrivals can be explained by mantle anisotropy. We attribute low V_s observed in the mantle north of the ridge to the presence of hydrous phases, resulting from the depth dependent dehydration of amphibole in an area where the slab is deeper.

TABLE OF CONTENTS

LIST OF FIGURES ……...…….. v

CHAPTER 1: INTRODUCTION ……..... 1

CHAPTER 2: TECTONIC SETTING ……. 4

CHAPTER 3: FIELD DEPLOYMENT AND DATA ……. 7

CHAPTER 4: METHODS ……... 9

CHAPTER 5: RESULTS ……... 12

CHAPTER 6: RESOLUTION TESTS …….. 14

CHAPTER 7: DISCUSSION …… 16

CHAPTER 8: CONCLUSION …….. 19

REFERENCES …….. 58

LIST OF FIGURES

Figure 1- Map of the South America showing the location of our study area ……..…..... 20

Figure 2- Map of the study area showing the major geomorphological features, station locations, and volcanoes ...……...…….…..... 21

Figure 3- Map showing initial earthquake locations calculated with SeisAn and final locations of earthquakes relocated as part of the inversion …….. 22

Figure 4- Map of final earthquake locations in our study area ...…….…… 23

Figure 5- Map of study area showing back azimuthal gap of final event locations ...…...…….. 24

Figure 6- Histogram of back azimuthal gap for used earthquakes ...……... 25

Figure 7- Scatter plot of residual values for all events ...……..… 26

Figure 8- Model versus data variance for different damping parameters …… 27

Figure 9- Model versus data variance for different numbers of iterations……... 28

Figure 10- Results of tomographic inversion at 45 km depth ……..… 29

Figure 11- Results of tomographic inversion at 55 km depth …….. 30

Figure 12- Results of tomographic inversion at 65 km depth …….. 31

Figure 13- Results of tomographic inversion at 75 km depth …….. 32

Figure 14- Results of tomographic inversion at 85 km depth ...…….…….. 33

Figure 15- Map showings locations for each cross-sections shown in Figures 16 – 25 ....…….. 34

Figure 16- Cross-section C-C’ ...…….…. 35

Figure 17- Cross-section D-D’ ……..... 36

Figure 18- Cross-section E-E’ ...…….……. 37

Figure 19- Cross-section F-F’ ……...…….……. 38

Figure 20- Cross-section G-G’ …….…….….... 39

Figure 21- Cross-section H-H’…….…….……..... 40

Figure 22- Cross-section I-I’…….……..…….... 41

Figure 23- Cross-section J-J’ ...……..……..…… 42

Figure 24- Cross-section K-K’ ……...…..... 43

Figure 25- Cross-section U-U’, oriented roughly parallel to the trench …….……. 44

Figure 26- Results showing the result of the checkerboard test at 45 km depth ……...…..…. 45

Figure 27- Results showing the result of the checkerboard test at 55 km depth ...……..……..... 46

Figure 28- Results showing the result of the checkerboard test at 65 km depth …….…… 47

Figure 29- Results showing the result of the checkerboard test at 75 km depth ..…….…… 48

Figure 30- Results showing the result of the checkerboard test at 85 km depth ...…….…. 49

Figure 31- Results showing recovery of anomaly A at 45 km depth in Vp ....……...……...…. 50

Figure 32- Results showing recovery of anomaly A at 45 km depth in Vs .....…….....…. 51

Figure 33- Results showing recovery of anomaly A at 55 km depth in Vp ...……..... 51

Figure 34- Results showing recovery of anomaly A at 55 km depth in Vs …….……..... 52

Figure 35- Results showing recovery of anomaly A at 65 km depth in Vp …...…..…….……...… 52

Figure 36- Results showing recovery of anomaly A at 65 km depth in Vs …...…….....…...…53

Figure 37- Results showing recovery of anomaly B at 45 km depth in Vp …...……..……...… 53

Figure 38- Results showing recovery of anomaly B at 45 km depth in Vs …...……..... 54

Figure 39- Results showing recovery of anomaly B at 55 km depth in Vp ……...…….…..... 54

Figure 40- Results showing recovery of anomaly B at 55 km depth in Vs ……...……...… 55

Figure 41- Results showing recovery of anomaly B at 65 km depth in Vp …...…….…...….. 55

Figure 42- Results showing recovery of anomaly B at 65 km depth in Vs …...……..…..….. 56

Figure 43- Results showing recovery region near anomaly C at 75 km depth in Vs …...…..... 56

Figure 44- Results showing recovery region near anomaly C at 85 km depth in Vs …...…..…. 57

Figure 45- Results showing recovery region near anomaly D at 75 km depth in Vs ...……57

CHAPTER 1: INTRODUCTION

Flat slab subduction refers to oceanic lithosphere that is subducting subhorizontally beneath the overriding continental plate. The western margin of South America includes three flat-slab regions: the Pampean flat slab in central Chile, the Peruvian flat slab in south central Peru, and the Bucaramanga segment beneath northern Columbia [Gutscher et al., 2000, Ramos and Folguera, 2009]. Flat slab subduction is commonly associated with the migration of volcanism away from the trench as the slab dip shallows, due to the displacement of asthenospheric corner flow in the mantle wedge [Gutscher et al., 2000, Ramos et al., 2002]. In South America, slab flattening has resulted in a total quiescence of volcanic activity in those regions where flat slabs occur.

Flat slab subduction has also been correlated with far-field, thick-skinned deformation, such as the Sierras Pampeanas in central Argentina. Flat slab subduction is often used to explain the development of inland uplifts and volcanic quiescence in earlier periods of orogenesis. For example, flat slab subduction is believed to have contributed to the thick-skinned deformation that uplifted the modern Rocky Mountains and a cessation in magmatism during the Laramide Orogeny [Dickinson and Snyder, 1978, Bird, 1984, Coney, 1987, Jordan and Allmendinger, 1986]. During that time the plate was horizontal.

Water released from the Farallon plate during the Laramide orogeny may have hydrated the mantle lithosphere of the North American continent [Humphreys et al., 2003, Dumitru et al., 1991]. After the removal of the Farallon slab, contact between hot asthenosphere and hydrated lithosphere resulted in extensive post-Laramide ignimbrite volcanism.

Several mechanisms have been proposed as causes for slab flattening. One possible cause is the subduction of aseismic ridges or oceanic plateaus [van Hunen et al., 2002, Gutscher et al., 2000]. According to the model of van Hunen et al. [2004], the overthickened oceanic lithosphere

includes a thick layer of harzburgite that is less dense than the mantle. The relative buoyancy of the ridge causes subduction to stagnate [Pilger, 1981]. Another proposed mechanism is that flat slabs are more buoyant because the ocean plate is relatively young [van Hunen et al., 2004, Cross and Pilger, 1978]. It has also been proposed that suction forces between the slab and the overriding continent may play a role, but theoretically this force would apply in all subduction zones and would require an already relatively shallow subducting lithosphere [Stevenson and Turner, 1977, van Hunen et al., 2004]. It has been suggested that a thick cratonic root could increase suction forces with subducting slabs, and result in trench rollback [Manea et al., 2011].

Body wave tomography conducted in central Chile-Argentina found low V_p, high V_s, and an unusually low V_p/V_s ratio above the Pampean flat slab between 30° and 36° [Wagner et al., 2005]. The correlation between the location of these seismic anomalies above the flat slab and the projected track of the Juan Fernandez ridge support the subduction of aseismic ridges as a cause of flat slab subduction. The results from Chile are not consistent with the hypothesis of Humphreys et al. [2003] that the mantle is hydrated above flat slabs. Wagner et al. [2008] argue that metasomatic formation of orthopyroxene in the cold overriding mantle could explain the observed velocity structure.

The Peruvian flat slab is younger in age, but the style of subduction is the same as that of Chile. Furthermore, both slabs are spatially related to subducting aseismic ridges. It is unknown whether the results from Chile are unusual to flat slabs or are the norm. As such, further research of flat slabs is required and the size and subduction style in Peru make that flat slab ideal for comparative study.

We employ regional travel time tomography for local earthquakes recorded on temporary arrays in Peru and northern Bolivia to investigate the seismic structure above the Peruvian flat slab.

Results indicate that the southern portion of the Peruvian flat slab above the ridge is characterized by low V_p and high V_s, similar to the pattern found above the flat slab in Chile [Wagner et al., 2005]. North of the ridge, a deeper Wadati-Benioff zone suggests a deepening of the flat slab. Here we find neutral/low V_p and low V_s that could indicate the presence of fluids or partial melts.

CHAPTER 2: TECTONIC SETTING

The continental crust of Peru records a complex tectonic evolution. The Arequipa-Antofalla terranes, between $8°$S and $26°$S include outcropping metamorphic basement of Paleoproterozoic age [Dalmayrac et al., 1977]. Cobbing et al. [1977] considered the Arequipa terrane to be associated with the Amazonia Craton. More recent studies have led to the proposal that these are allocthonous terranes which were amalgamated to the proto-South American margin [Monger et al., 1982, Coira et al., 1982, Ramos, 2008]. The formation of Rodinia during the Grenville orogeny involved the coming together of Laurentia and the Amazonian and Pampean terranes. The Arequipa and Antofalla blocks represent oceanic volcanic arcs that were caught between the proto-continents during the closing of the intracontinental oceans [Ramos, 2008]. These blocks may have wholly or partly rifted from Amazonia and Pampia during the breakup of Rodinia and re-accreted later under convergence associated with the formation of Gondwana [Vaughan et al., 2005, Ramos, 2008]. Subsequently, the Arequipa terrane underwent minor rifting and back arc basin formation during the break-up of Gondwana, but remained attached to the South American margin [Ramos, 2008].

There are five distinct geomorphological units in Peru (Figure 2): the coastal forearc, the Western Cordillera, the Altiplano, the Eastern Cordillera, and the Subandean zone [Ramos and Folguera, 2009, Dorbath, 1996]. The previously mentioned Arequipa terrane outcrops along the coastal plain [Ramos, 2008]. The Arequipa terrane is likely more mafic in composition than the adjacent Western Cordillera [Mamani et al., 2008]. Within the Arequipa terrane, outcrops of the basement rocks along the coast are characterized as granulite facies dioritic gneisses and strongly foliated mafic meta-igneous rocks [Ramos, 2008]. The Andean batholith outcrops just east of the coastal forearc. The batholith is characterized by Paleozoic granitic rocks emplaced during subduction associated with Famatinian volcanic arc. East of the Andean batholith, north of $12°$S,

the Andean topography resembles a normal arc cordillera. South of $12°$S, the Western and Eastern Cordillera are separated by the Altiplano plateau [James, 1971]. The Western Cordillera, or Cordillera Occidental, is a subduction related volcanic mountain belt comprised of Quaternary volcanics with outcrops of older Miocene and Pliocene volcanic structures [Mamani et al., 2008, James, 1971]. Mišković and Schaltegger [2009] identify the rocks of the Western Cordillera as felsic-intermediate plutonic rocks and volcanics. The Eastern Cordillera is older than the Western Cordillera, comprised of metamorphosed Paleozoic sedimentary rocks cut by Cenozoic and Mesozoic intrusives [Roperch et al., 2011, James, 1971]. The Altiplano, which separates the Western and Eastern Cordilleras, south of $12°$S, is an internally drained sedimentary basin, with up to 30 km of accumulated sediments in the central part of the basin [James, 1971]. The various geomorphological features described are illustrated in Figure 2. The Peruvian flat slab region underlies some of the highest elevations in the Andes. The second highest peak in South America sits above the flat slab in the Cordillera Blanca, located to the north of our study area. The Cordillera Blanca and the Maranon Massif to the east belong to a basement uplift of metamorphic core complex similar to the Sierras Pampeanas in Argentina [Ramos and Folguera, 2009].

The Peruvian flat slab is located between $5°$S and $14°$S. In this region, the Nazca plate initially subducts normally to some depth before it bends and traverses horizontally beneath the overriding plate [Gutscher et al., 2000, Ramos and Folguera, 2009, Cahill and Isacks, 1992]. Sub-horizontal subduction continues for several hundreds of kilometers before the slab descends further into the mantle. Geological features commonly associated with flat slab subduction, such as the basement uplift of the Cordillera Maranon and the migration and cessation of arc volcanism, are observed above the Peruvian flat slab [Ramos and Folguera, 2009, Aleman, 2006].

Radiometric dating has shown an eastward migration in Cenozoic magmatism in Peru [Aleman, 2006]. Active volcanism ended around 12 Ma, coinciding approximately with the arrival of the Nazca ridge, which began subducting 11.2 Ma around $11°$S according to plate reconstructions [Hampel, 2002]. Subduction has since migrated southward, to where the Nazca ridge currently subducts beneath South America at $15°$S. The ridge is a bathymetric high 200 km wide and 1.5 km high, trending N42E at $15°$S. Over the last $\sim$5 Ma, average convergence rates between the Nazca plate and the South American plate have been estimated as 75 mm/yr at $12°$S and 78 mm/yr at $22°$S [Somoza, 1998]. Somoza [1998] predicts plate motions based on the NUVEL-1D model of DeMets et al. [1990]. Average convergence azimuth is N77°E at $12°$S and N$74°$E at $22°$S [Somoza, 1998]. Collision of the ridge with the continental margin is responsible for the narrowed shelf and elevated marine terraces [Hampel, 2002]. Hampel [2002] interprets the collapse of earlier marine terraces to the north as evidence of the southward progression of the ridge. Inland projections of the Nazca ridge place it beneath the location the Abancay Deflection at the northern boundary of active volcanism. The Abancay deflection, a large scale crustal block rotation, is responsible for considerable structural offsets in the Peruvian Andes [Roperch et al., 2011]. Figure 2 shows the location of the Abancay deflection and its relative location to the Nazca ridge. Block rotations in Peru have been observed to be counterclockwise in orientation [Roperch et al., 2011, Mitouard et al., 1992, Macedo-Sánchez et al., 1992, Roperch and Carlier, 1992].

CHAPTER 3: FIELD DEPLOYMENT AND DATA

This study incorporates data recorded at 57 temporary stations from three seismic net- works in Peru and Bolivia: PULSE, CAUGHT, and PERUSE. The PerU Lithosphere and Slab Experiment (PULSE) consists of 40 broadband seismometers deployed above the flat slab in south-central Peru from 2010-2013. Data were collected at a rate of 40 samples per second using a combination of Nanometrics Trillium 120 sensors with Taurus data- loggers and Güralp CMG-3T sensors with Quanterra Q330 data loggers. The stations were deployed in three transects oriented approximately trench normal. The northern transect extends northeast from Lima, situated above the location where subduction of the Nazca ridge occurred 10-8 Ma. The central transect connects Pisco and Ayacucho. This line of stations is located along the northern edge of the projected location of the subducted Nazca ridge today. The southern transect corresponds roughly to the projected location of the southern edge of the subducted Nazca ridge. Additionally, there are two lines oriented trench parallel; one situated along the coast, and the other connecting the centers of the northernmost two lines.

The Central Andean Uplift and Geodynamics of High Topography (CAUGHT) project consists of 48 stations deployed in southern Peru and northern Bolivia from 2010-2013. Data were collected with STS-2 sensors and recorded on Quanterra Q330 data loggers. This study incorporates events recorded at 11 CAUGHT stations north of $15°$S and west of $-70°$. These stations are included because they are close enough to the flat slab that they record many of the events we use. This provides a useful augmentation to the data set. The PERU Slab Experiment (PERUSE) project is a collaboration between the Tectonics Observatory at Caltech, the Center for Embedded Network Sensors (CENS) at UCLA, and the Instituto Geofisico del Peru (IGP). An arrangement with the PERUSE project allows us to include data from 8 of these stations. The data were col-

lected using Güralp CMG-3T sensors with a combination of Quanterra Q330 and Reftek RT-130 data loggers, sampled at a rate of 100 sps.

The tomographic study presented here uses 277 events recorded between May 2011 and May 2013 (Figure 4). I picked P- and S- wave arrival times using the SeisAn Earthquake Analysis Software [Havskov and Ottemoller, 1999, Ottemoller et al., 2013]. Initial locations were calculated based on P-waves only. These locations were then used to rotate the components into radial and transverse, and first arrival S-waves were picked on the transverse component. The events were then relocated using both P- and S- arrivals. I included only earthquakes with azimuthal gaps less than $270°$. This comparatively large ($> 180°$) azimuthal gap was selected as the cut off due to the sparsity of seismicity within the flat slab, particularly along the eastern margin of the study area. We perform resolution tests to determine if the inclusion of events with azimuthal gaps larger than $180°$ significantly alters our results (see Chapter 6: Resolution Tests). In general, we find that adding these events improves resolution in our area of interest but does not change the dominant features discussed here. Figure 5 shows the map of events plotted according to back azimuthal gap. A histogram of back azimuthal gaps for all events is shown in Figure 6.

CHAPTER 4: METHODS

We invert simultaneously for V_p and V_s using the method of Zhao et al. [1992]. This method improves ray tracing by including a-priori information about discontinuities, and the location of the subducting slab. Snell's law is applied to more accurately trace ray paths across discontinuities. The pseudo-bending technique of Um and Thurber [1987] is used to calculate ray paths between discontinuities. The starting velocity model incorporates three discontinuities. We assign the first two discontinuities depths of 1 and 2 km respectively, but we do not assign velocity changes along these discontinuities. We separate the area of interest into two grids (A and B) based on the depth of the third discontinuity. The third discontinuity in our study is the Moho. The depth to the Moho at a given location determines whether a given grid node is in the A grid or the B grid. Each grid node is assigned the correct starting velocity according to whether the node is in the crust or in the mantle. The benefit of this technique is that the adjustment of the A grid is independent of the B grid and vice versa. This allows velocity deviations to vary abruptly across the Moho, allowing us to differentiate between crust and mantle structures.

Receiver function studies indicate that the slab and the continental plate are coupled along the trench [Hayes et al., 2012]. The dipping interface between the continental and oceanic crusts extends from the trench to approximately 40 km depth beneath the coast. We constructed a Moho model using results from the density measurements of Tassara et al. [2006], but with crustal thicknesses near the coast increased from $\sim$10-20 to 40 km. Using the plate boundaries defined by Bird [2003], we set the Moho west of the trench equal to 10 km depth. Starting velocities for the crust and mantle were taken from James and Snoke [1990]. Above the Moho, we use starting P- and S-wave velocities equal to 6.27 and 3.5 km/s, respectively. Below the Moho, starting velocities for P- and S- waves are 8.0 and 4.48 km/s, respectively. We relocate events at the beginning of each

iteration using the new velocity model, and calculate travel times through the new model using the new locations. Travel time residuals are calculated by taking the difference between the calculated travel times and the travel times based on our picks. P- and S- picks with residuals greater than 2.0 seconds are considered to be outliers based on scatter plots of the residuals shown in Figure 7, and are removed from the inversion. Our grid has 40 km x 40 km horizontal node spacing and 10 km vertical node space up to 150 km depth.

The damping parameter controls how much the model is allowed to vary from the starting model with each iteration. Damping is used to reduce the impact of noise and stabilize the inversion process [Menke, 1984]. Decreasing the damping parameter will reduce travel time residuals while increasing model length; increasing the damping parameter will result in reduced model parameters but increased data variance. To select the damping parameter, we perform one iteration of our inversion for each of a suite of damping values and plot data variance versus model variance for each damping parameter used. This results in a curve showing the trade-off between data and model variance (Figure 8). The damping parameter is chosen based on a balance between goodness of fit and model size. We have selected a damping parameter of 35 for our inversion.

There is a similar trade-off between model and data variance for the number of iterations performed. Multiple iterations increase the variance in the model as the inversion seeks to more closely represent the data. A model that includes large velocity deviations may be best for reducing residuals, but is not necessarily realistic. We performed an inversion with a damping parameter of 35 for 10 iterations and calculated model and data variance at each step. Variance values, equivalent to the residual sum of squares (RSS), are shown in Figure 9. The damping value and the number of iterations did not substantially change the patterns in our result, only the intensity of the velocity deviations. At the first iteration, data variance is 0.60493 seconds and model variance

is zero. After 4 iterations, data variance is 0.38046 seconds and model variance is 3.9795. Using a damping parameter of 35 and 4 iterations resulted in a 40% reduction in the RSS. The RSS is calculated by squaring the travel time residual for each used pick and taking the sum of these values divided by the number of observations (see Equation 1).

$$RSS = \frac{\sum (x_i^2)}{n_{obs}} \tag{1}$$

I calculated the percent improvement by taking the difference between the initial and final RSS values divided by the initial value and multiplied by 100 (see Equation 2).

$$\%improvement = \frac{initial - final}{initial} \times 100 \tag{2}$$

The root mean square (RMS) of the travel time residuals at initial and final iterations was calculated by taking the square root of the RSS at initial and final steps (see Equation 3). Improvement of the RMS value was 22%.

$$RMS = \sqrt{\frac{\sum (x_i^2)}{n_{obs}}} \tag{3}$$

CHAPTER 5: RESULTS

We present results in map view for 45, 55, 65, 75, and 85 km depth slices for which we have reasonably good resolution (Figures 10-14). Resolution at greater depths is limited due to the shallow ($<$ 90 km) hypocentral depth of most of our events. Shallower depths are subject to vertical streaking. The most robust anomalies (labeled A, B, C, and D in 10-14) are discussed below.

Anomaly A is shown in map view for tomography results at 45-65 km depths in Figures 10-12 and in cross-section view in Figures 17-21. This is a crustal anomaly, characterized by large positive deviations in V_p and V_s in the center of our study area. The absolute velocities of this anomaly range from 6.4 to 6.6 km/s for P-waves and 3.6 to 3.8 km/s for S-waves.

Anomaly B is shown in map view for tomography results at 45-65 km depths in Figures 10-12 and in cross-section view in Figures 17-21. This anomaly is located below the continental Moho, either in the continental mantle lithosphere or in the oceanic lithosphere. It exhibits positive V_p and V_s deviations and is oriented parallel to the trench. At 45 km, absolute V_p for this anomaly is between 8.2-8.6 km/s, and absolute V_s ranges between 4.6-4.8 km/s. The location of Anomaly B at 45 km corresponds to the 40 km slab contour from Hayes et al. [2012]. Anomaly B is less prominent at 55 km depth. Fast velocity deviations appear clearly north of $\sim$ 14°S and south of 16°S. In between, velocity deviations are close to neutral, with modestly fast V_p and modestly slow V_s (Figure 11); These deviations, however, are less than $\pm 1\%$. At 65 km, we see fast V_p and V_s located near the 60 km slab contour from Hayes et al. [2012]. Absolute velocities are 8.2-8.3 km/s for V_p and $\sim$ 4.6 km/s for V_s (Figure 12).

Anomaly C is shown in map view at 75 and 85 km depth in Figures 13-14 and in cross-section view in Figures 21-24. Anomaly C is characterized by neutral or slow V_p and fast V_s in

the mantle above the southern portion of the flat slab. At 75 km, we observe this anomaly between $13°$S and $\sim$ $16°$S, and between $\sim$ $75°$W and $72°$W. Deviations at 75 km in V_s correspond to absolute velocities of 4.6-4.8 km/s. Maximum negative deviations in V_p, around -4%, align with the southern corner of the flat slab according to the slab model of [Hayes et al., 2012]. We also observe slow V_s in this region, south of Anomaly C. There is a relatively small low velocity zone located within Anomaly C at 75 km, that corresponds approximately to the location of Sara Sara volcano in southern Peru, shown in Figure 2 [Siebert and Simkin, 2002]. We observe Anomaly C continues to 85 km, again with slow-neutral V_p and fast V_s. Absolute velocities for V_s range between 4.6 and 4.8 km/s.

Anomaly D is shown in map view at 75 and 85 km depths in Figures 13-14 and in cross-section view in Figures 16-20. Anomaly D, located in the northern section of the flat slab, is characterized by neutral V_p and slow V_s. At 75 km depth, absolute V_s ranges between 4.2 and 4.4 km/s. Deviations are more modest at 85 km, with absolute V_s between 4.4 and 4.5 km/s.

CHAPTER 6: RESOLUTION TESTS

To test the resolution of our study area, we first use checkerboard tests. We create a velocity model that has $\pm 5\%$ deviations at each grid node, alternating in a checkerboard pattern. We calculate predicted travel times through the checkerboard model. The synthetic data set is then inverted using our initial starting model to see if the checkerboard pattern can be recovered. The recovered V_p and V_s pattern is poor at shallow and intermediate crustal depths. The checkerboard has the best recovery at 45, 55, 65, 75 and 85 km.

Recovery of the checkerboard is limited at 45 and 55 km for the region associated with Anomalies A and B. We observe much better recovery of the checkerboard for these anomalies at 65 km. For Anomaly C, the checkerboard is well recovered in V_p and V_s at 75 km and somewhat recoverable at 85 km. The checkerboard recovery of Anomaly D is fairly poor for both V_p and V_s (Figures 26-30).

We also investigate the reliability of our anomalies using recovery tests. For the recovery tests, we create specific anomalies of different shapes and sizes with either a positive or negative 5% deviation. We calculate the predicted arrival times through the starting model that incorporates the velocity anomalies, and use the predicted arrivals with our original velocity model to see if the anomalies can be recovered.

Figures 31-36 show recovery of anomalies roughly contingent with the location of our Anomaly A. We see that deviations are mostly recovered for the region northwest of the southern line of PULSE stations, but recoverability declines to the southeast due to insufficient ray coverage. Results for recovery tests of anomalies that correspond approximately to the location of Anomaly B are shown in Figures 37-42. We observe good recovery at 45 km depth. Anomalies at 55 and 65 km are reasonably well recovered. Results for recovery tests of an anomaly modeled after Anomaly C

are shown in Figures 43-44. We find there is decent recovery of the anomaly at both 75 and 85 km depth. Results for the recovery of an anomaly approximating our Anomaly D (Figure 45) show that the deviations are somewhat recoverable, although resolution decreases to the northwest.

CHAPTER 7: DISCUSSION

Much of the lower crust above the flat slab is characterized by fast V_p and V_s (Anomaly A; Figures 10-12) consistent with the displacement of hot asthenospheric corner flow due to the flattening of the subducted Nazca plate. Geothermal models of flat slabs by English et al. [2003] have shown that temperatures above mature flat slabs can be as low as 300°C. We also see high velocities following the coast in the mantle lithosphere at 45 and 65 km associated with Anomaly B. Anomaly B correlates well to the location of the subducting slab [Hayes et al., 2012].

We observe neutral to slow V_p and fast V_s at 75 and 85 km above the southern portion of the flat slab (Anomaly C). The slab 1.0 model of Hayes et al. [2012] suggests that flat slab regions in this area range between approximately 80 km in the north to around 100 km in the south. Our local earthquake locations in this region range between 75 and 85 km depth. Given errors in vertical depth, it is difficult to determine whether we are imaging the slab or overriding mantle lithosphere. The low V_p and high V_s is similar to the results of the body wave tomography study of the Chilean flat slab [Wagner et al., 2005, 2008]. Wagner et al. [2008] proposed, based on the seismic studies of Hacker et al. [2003], that metasomatism of mantle rocks through the influx siliceous fluids from the subducting slab could result in the observed velocities. More recent studies have focused on anisotropy of mantle peridotites to explain faster than expected S-wave arrival times [Hacker and Abers, 2012]. Due to the ray geometry defined by the flat slab, the S-wave arrivals used in this study are SH waves. It is expected that subhorizontal orientation of the slab should result in subhorizontal flow in the mantle [Hacker and Abers, 2012]. If mantle minerals are aligned preferentially so that their fast polarization directions lie in the horizontal plane, this could account for faster than expected shear wave velocities. Future investigations of SV velocities from inversions of Rayleigh waves will help to resolve this issue.

North of Anomaly C, there is little deviation in V_p and unusually low V_s, which we refer to as Anomaly D. This low V_s anomaly is reasonably well resolved at 75 km. One proposed mechanism for this is that there is a tear in the slab. Slab tearing has been noted in at least in one instance in Japan, but in that case the slab tearing occurred at 650 km depth as a result of flattening along the discontinuity [Obayashi et al., 2009]. Barazangi and Isacks [1976] suggested a possible tear in the Pampean flat slab based on teleseismic earthquake locations, though this tear was located further to the south where there is an abrupt change in slab geometry. Others have argued against this, using local seismicity as evidence that the slab is continuous but flexed [Cahill and Isacks, 1992, Hasegawa and Sacks, 1981, Schneider and Sacks, 1987]. Local seismicity in our area appears to be continuous from south to north, consistent with a continuous plate to the south of the Nazca Ridge. North of the Nazca ridge, the low shear wave velocities may indicate the presence of a sag in the slab. Earthquake hypocenters in this area range between 90 and 110 km depth close to the coast. This is distinctly different from the 60 and 80 km slab depth proposed by Hayes et al. [2012] (see Figure 4). The Nazca ridge has migrated south over the last 11 Ma to its current location at $\sim 15^{\circ}$S. Currently its location corresponds to the flattest part of the slab as evidenced both by seismicity and tomographic results. If we accept that the Nazca ridge plays a role in the development of flat subduction, then the slab north of the ridge may no longer be positively buoyant and may be beginning to sink. Gutscher et al. [2000] proposed that the along-strike extent of the Peruvian slab was due to the subduction of the Inca plateau to the north of the Nazca ridge. If this is true, the plateau is now completely subducted. Gutscher et al. [2000], however, does refer to a sag north of our study region, which he justified with earthquake locations and travel-time tomography; He explains the sag as a region of the slab between the subducted Inca plateau and the Nazca ridge that is less buoyant, a mechanism that would agree with our findings. We hypothesize that the

lower V_s seen in the north (Anomaly B) may indicate a relaxation of the slab, after the ridge has passed. Phase equilibria diagrams from English et al. [2003] indicate that in normally subducting slabs, dehydration of amphibole occurs between 60 and 80 km at temperatures ranging 300-800°. If we accept a sagging slab geometry north of the Nazca ridge, then Anomaly D may be explained by dehydration of the subducting oceanic lithosphere.

CHAPTER 8: CONCLUSION

We see high velocities in the lower continental crust (Anomaly A) that are consistent with thermal shielding produced by the flat slab, as modeled by English et al. [2003]. We also see evidence of the subducting slab along the coast at 45 and 65 km (Anomaly B). We observe low V_p and high V_s at 75-85 km located in the region of the subducting Nazca ridge, in the southern portion of our study area (Anomaly C). The close resemblance of this pattern to the results of Wagner et al. [2005, 2008] for similar studies of the Pampean flat slab, lead us to believe that the high V_s we observe could possibly be related to a metasomatized remnant of the lithospheric mantle above the slab (Anomaly C). However, earthquake locations suggest that there is little or no lithospheric mantle in this region. Another hypothesis is that the fast S-wave arrivals can be explained by mantle anisotropy [Hacker and Abers, 2012]. Earthquake locations north of the Nazca ridge suggest that slab is deeper north of the Nazca ridge. The continuity of seismicity along the length of our study area argues against slab tearing. We suggest that low V_s observed in the mantle north of the ridge (Anomaly D) could be due to presence of hydrous phases, resulting from the depth dependent dehydration of amphibole in an area where the slab is deeper.

Figure 1: Map of the South America with Nazca slab contour lines at 20 km intervals [Hayes et al., 2012]. Our study area is delineated by the red box. A close up of this region is shown in (Figure 2).

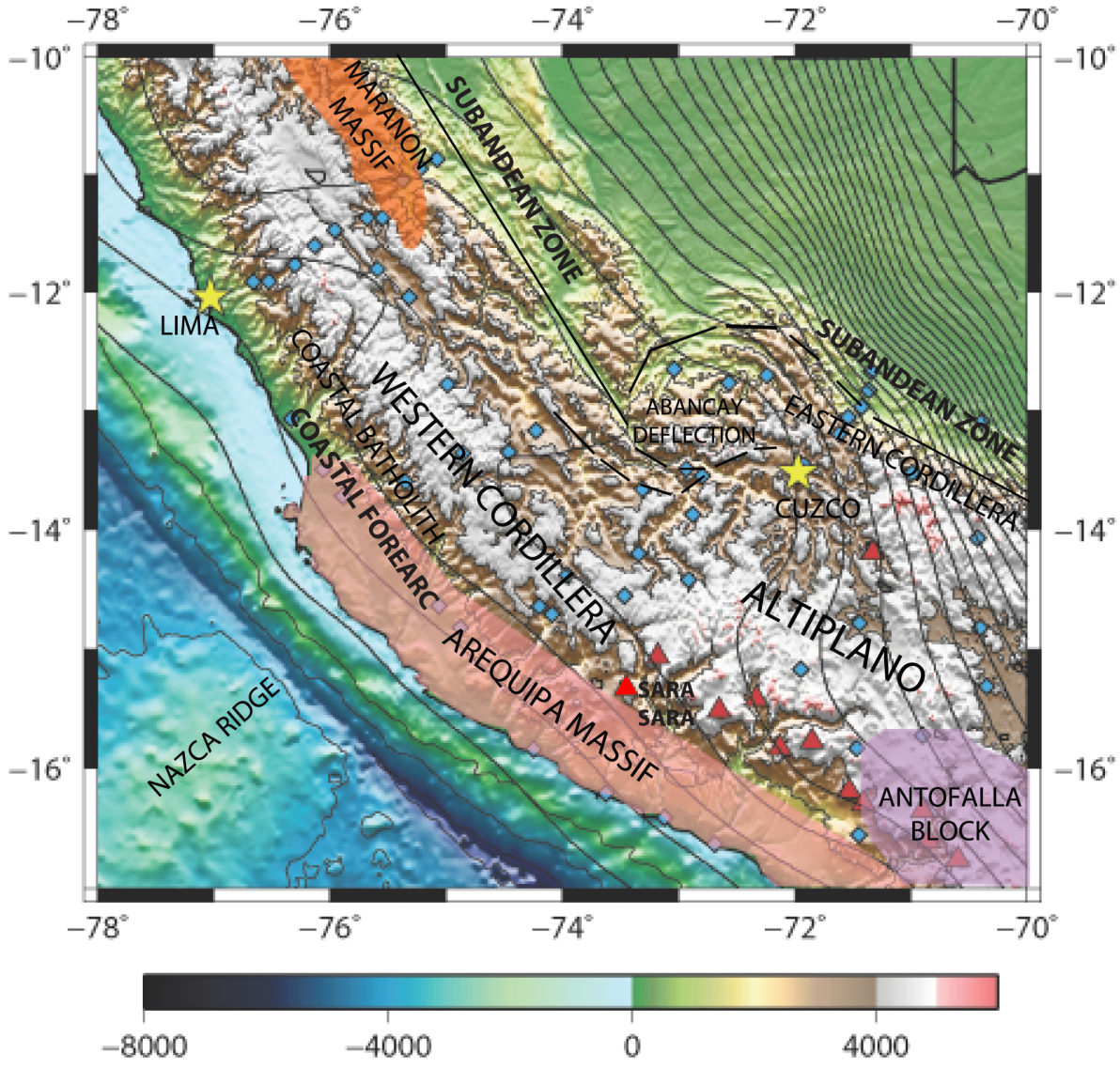

Figure 2: Map of the study area showing the five major geomorphological features of the region as oulined by Ramos and Folguera [2009], Dorbath [1996]: the Coastal Forearc, Western Cordillera, Altiplano, Eastern Cordillera, and the Subandean Zone. The cities of Lima and Cuzco are represented by gold stars. Blue diamonds indicate the locations of stations. The locations of volcanoes are indicated by red triangles. The location of Sara Sara volcano is illuminated as a bright red triangle. We have also labeled the locations of the Arequipa and Antofalla blocks described by Ramos [2008], the Maranon Massif [Ramos and Folguera, 2009], the Nazca Ridge, and the Abancay Deflection [Roperch et al., 2011].

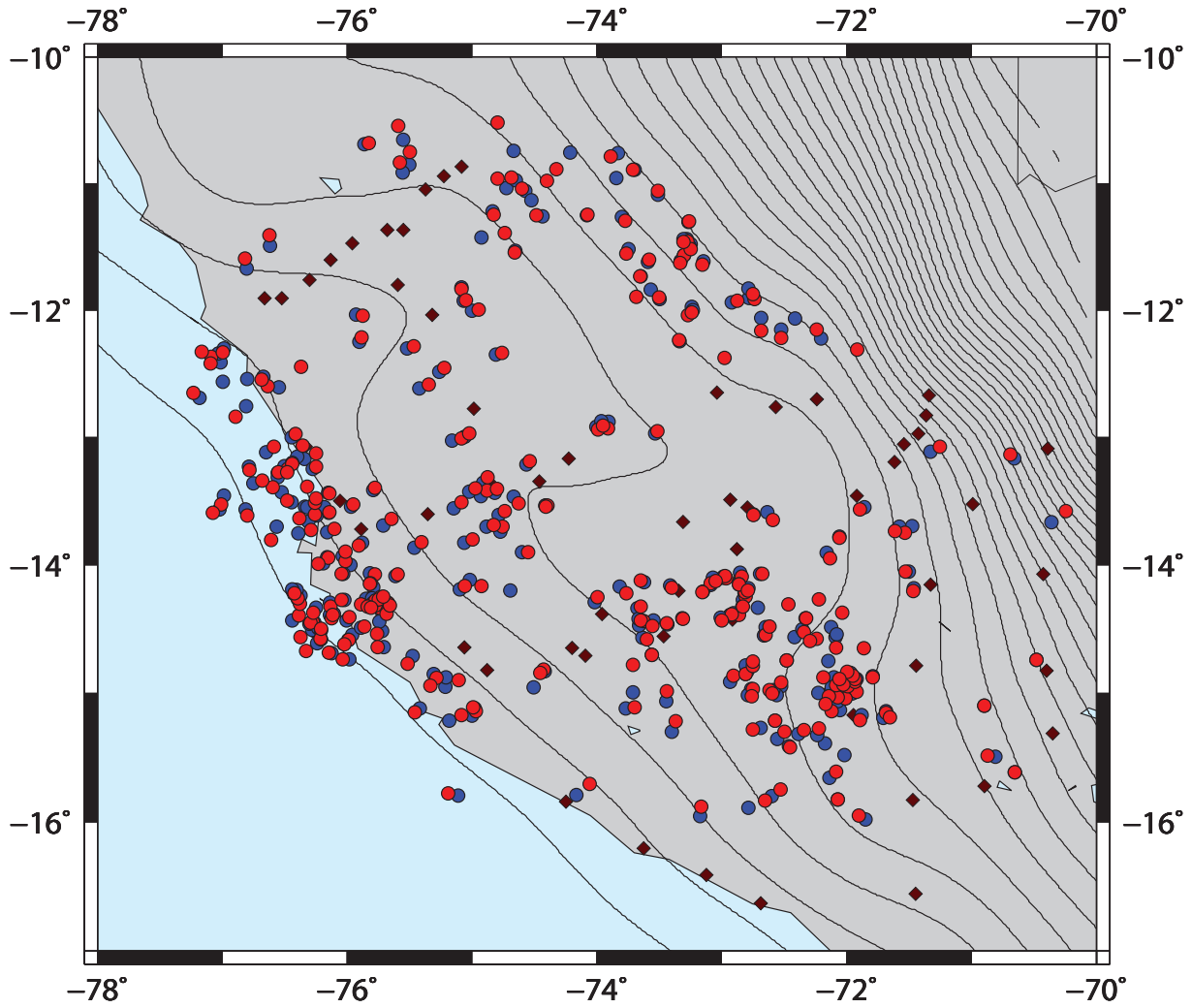

Figure 3: Map showing earthquake relocations within the study area. Blue circles respresent the initial locations calculated with SeisAn using hand picked first arrivals on the vertical (P-wave) and transverse (S-waves) components. Red circles represent the final locations of earthquakes relocated as part of the inversion. Contours indicate the location of the top of the subducting slab according to the slab 1.0 model of Hayes et al. [2012]. Contours start at 20 km off shore and increase by increments of 20 km. The locations of the stations used in this studied are shown as dark red diamonds.

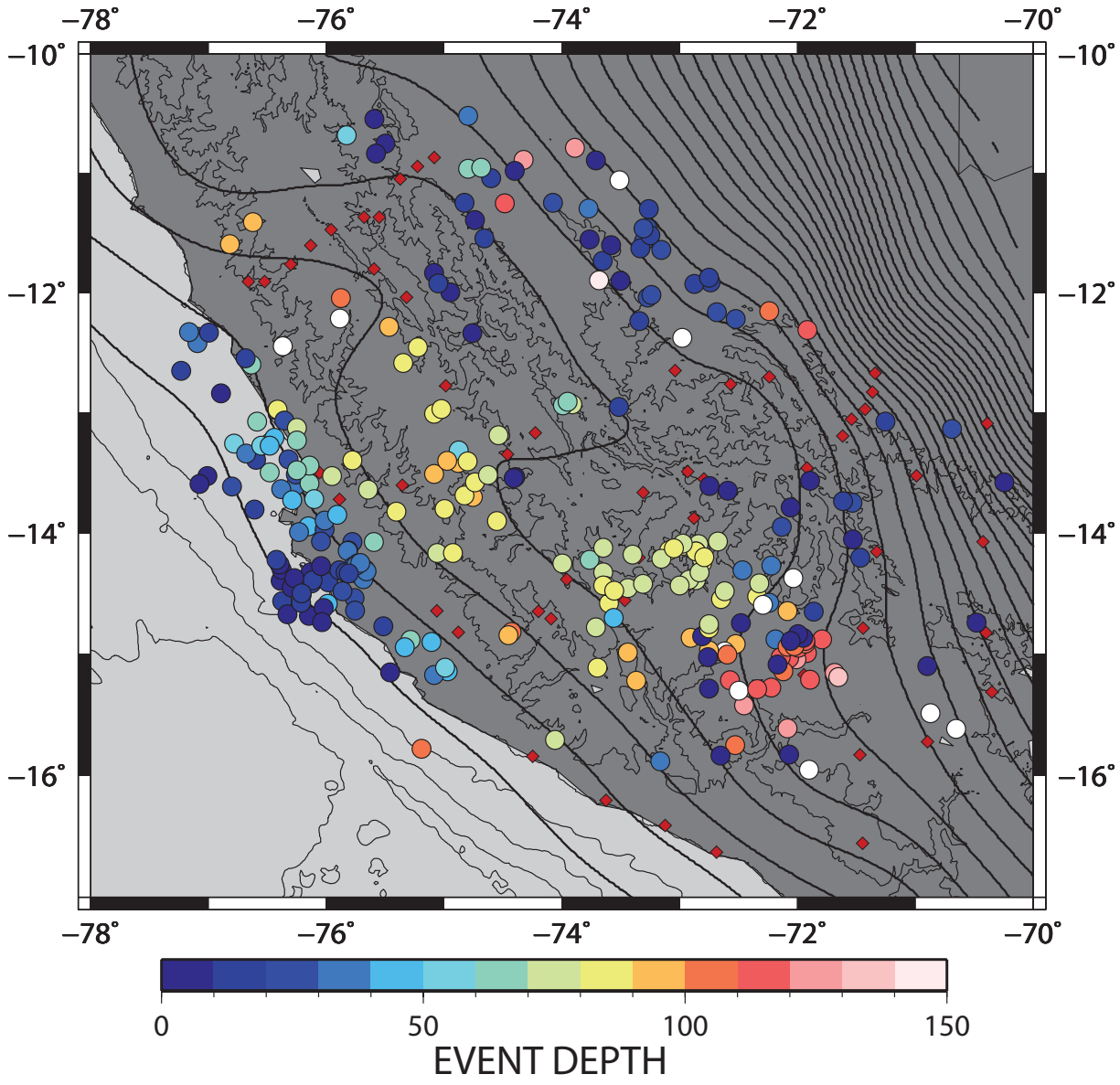

Figure 4: Map of final earthquake locations in our study area. The circles represent 277 events relocated with the inversion, after four iterations. The colors of the circles indicate the depths of the events.

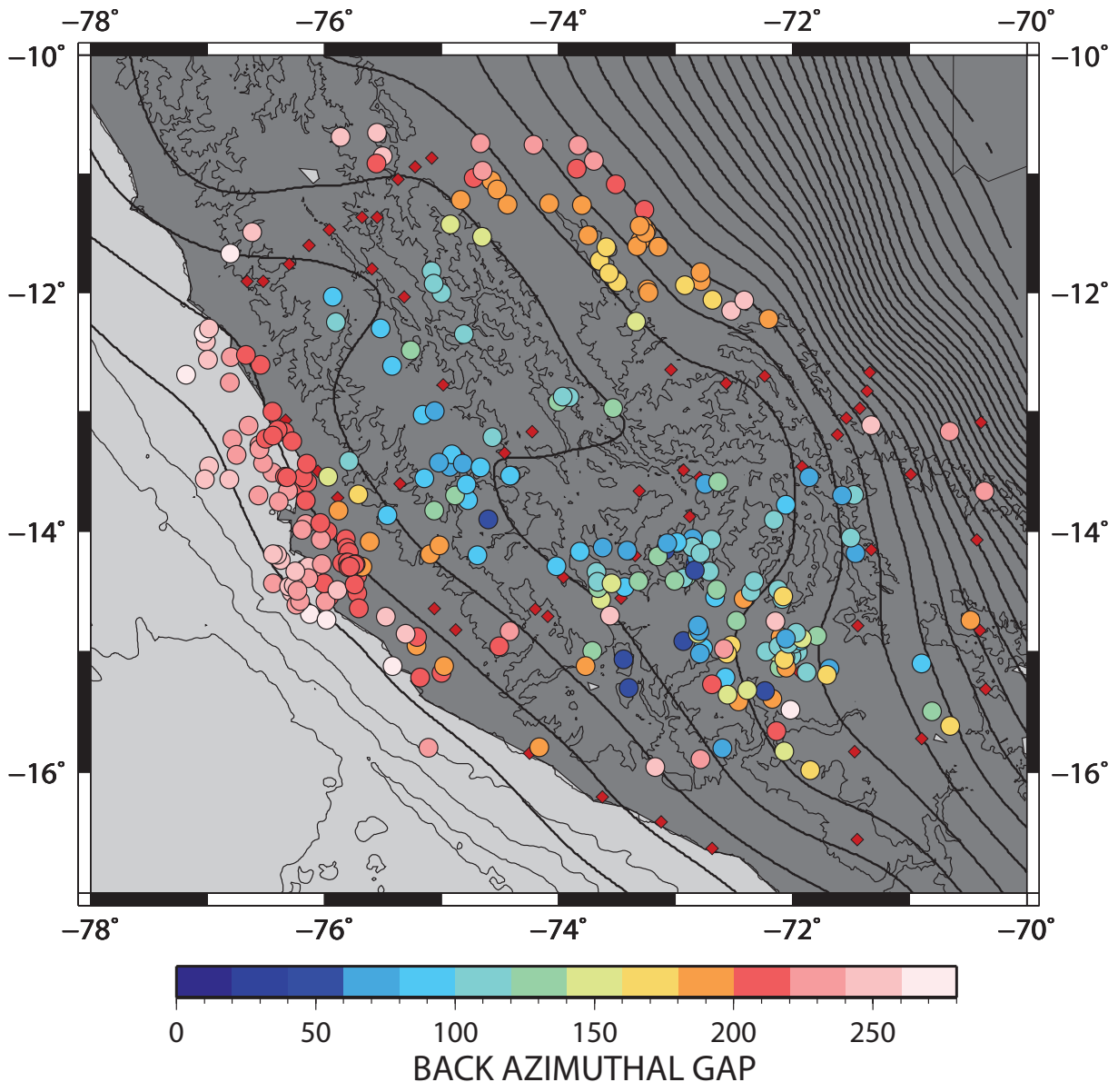

Figure 5: Map of study area with circles representing final event locations for 277 events used. The circles are coloered according to back azimuthal gap.

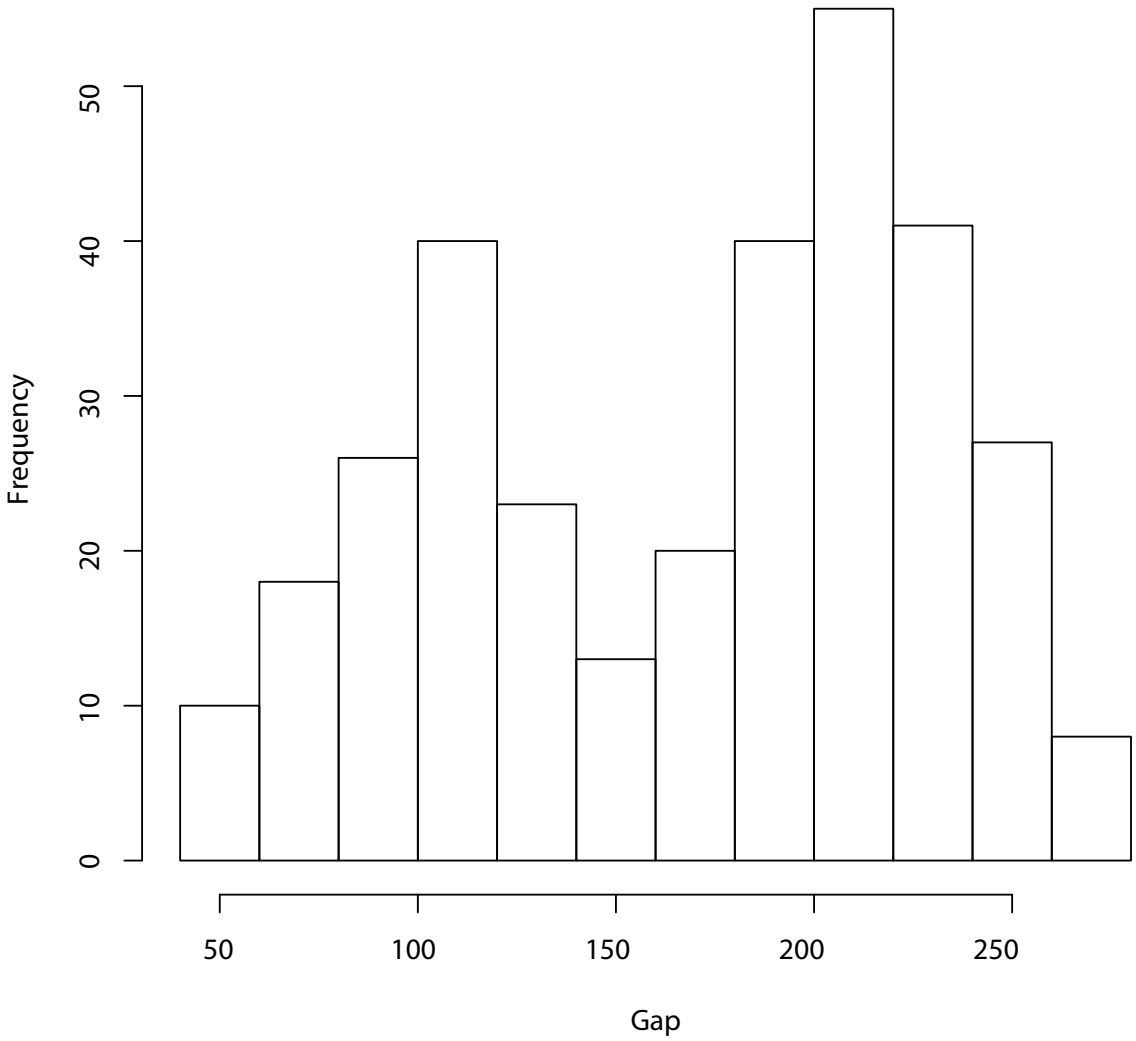

Figure 6: Histogram of back azimuthal gap for events in this study. We decided to allow the use any event with gap less 270.

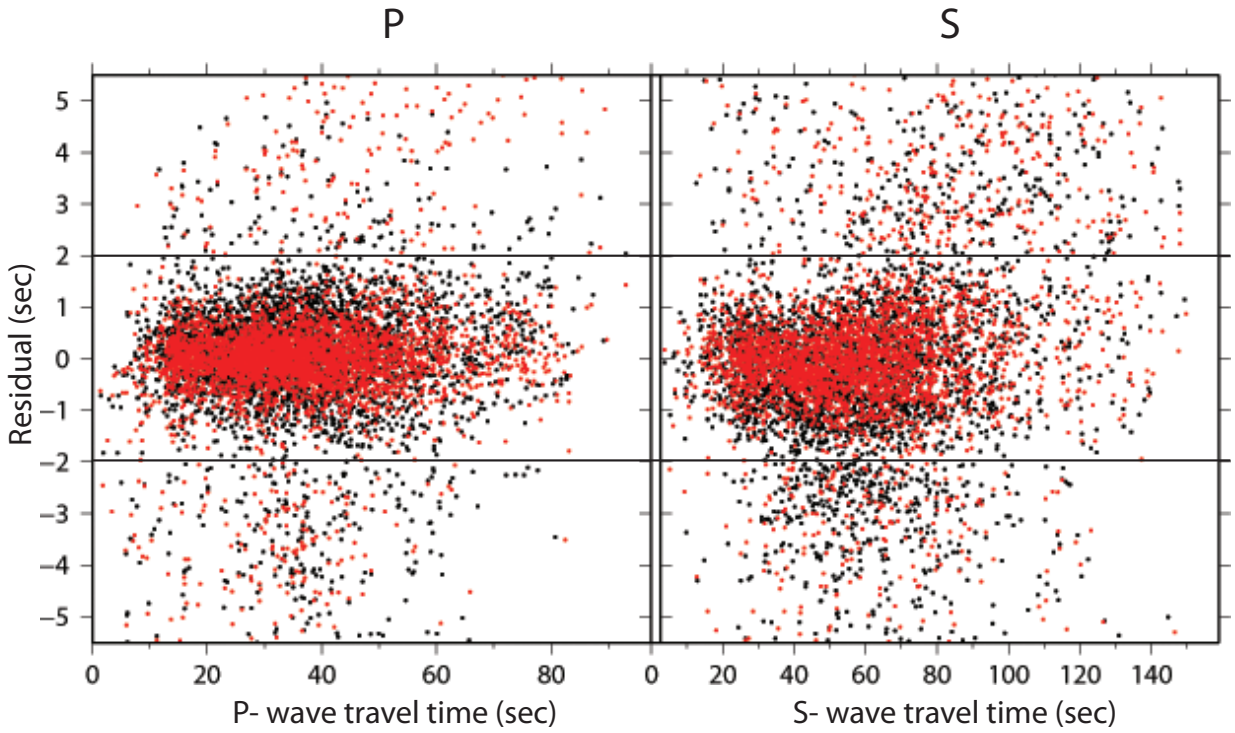

Figure 7: Scatter plot of residual values for all events. Residual values after the first iteration for P (left) and S (right) are shown in black. Final residuals after the fourth iteration for P (left) and S (right) are overlain in red. Only picks with residual values less than 2 seconds were used in the inversion.

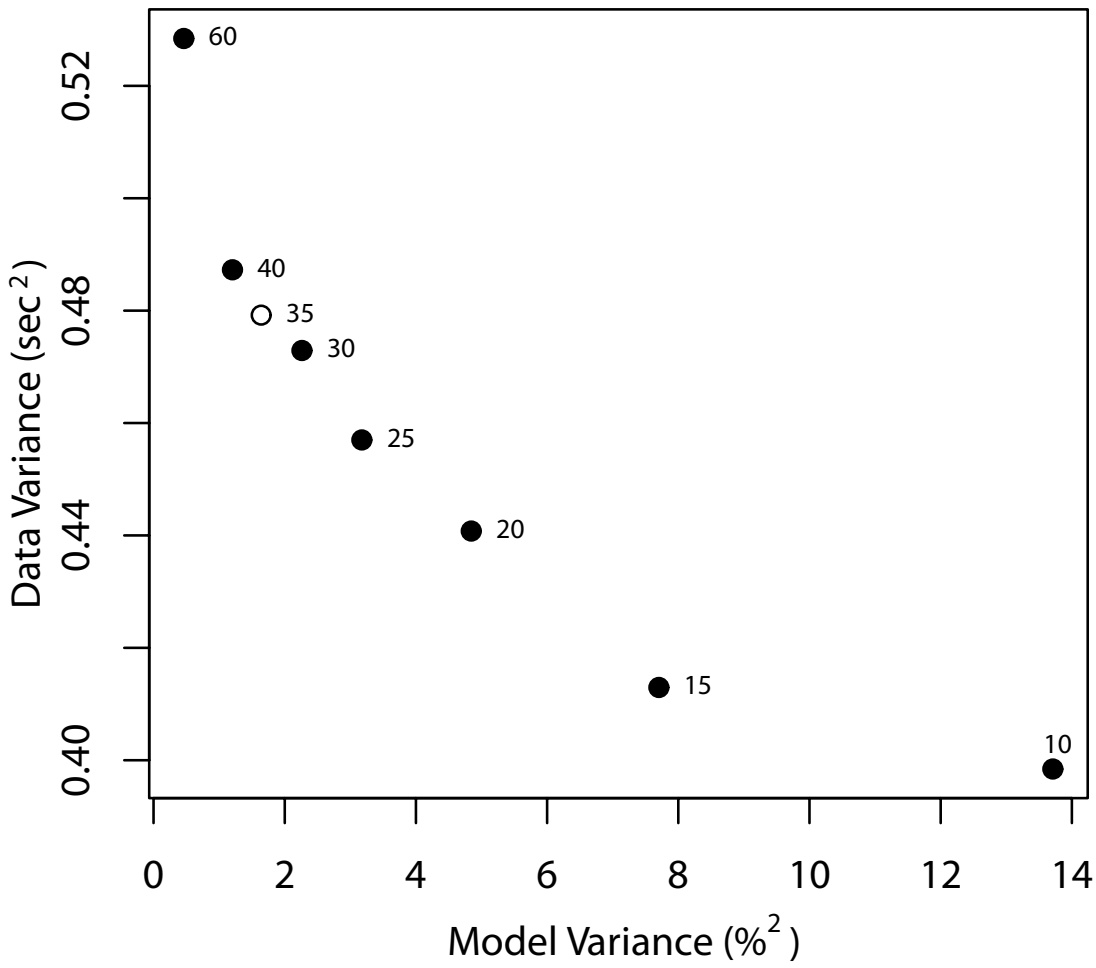

Figure 8: Model versus data variance for different damping parameters. We selected a damping parameter equal to 35 for use in the inversion.

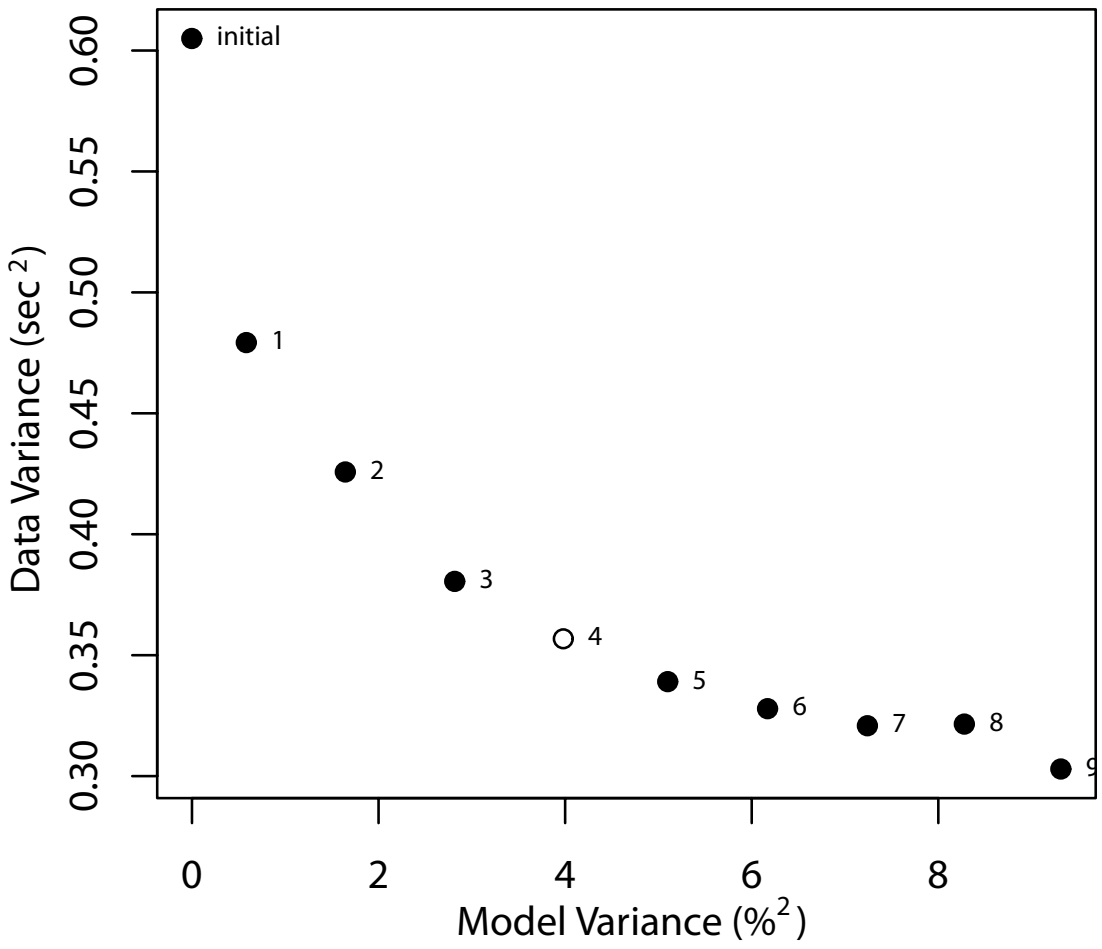

Figure 9: Model versus data variance for different numbers of iterations. We chose to use four iterations with damping equal to 35 to minimize variance in both data and model.

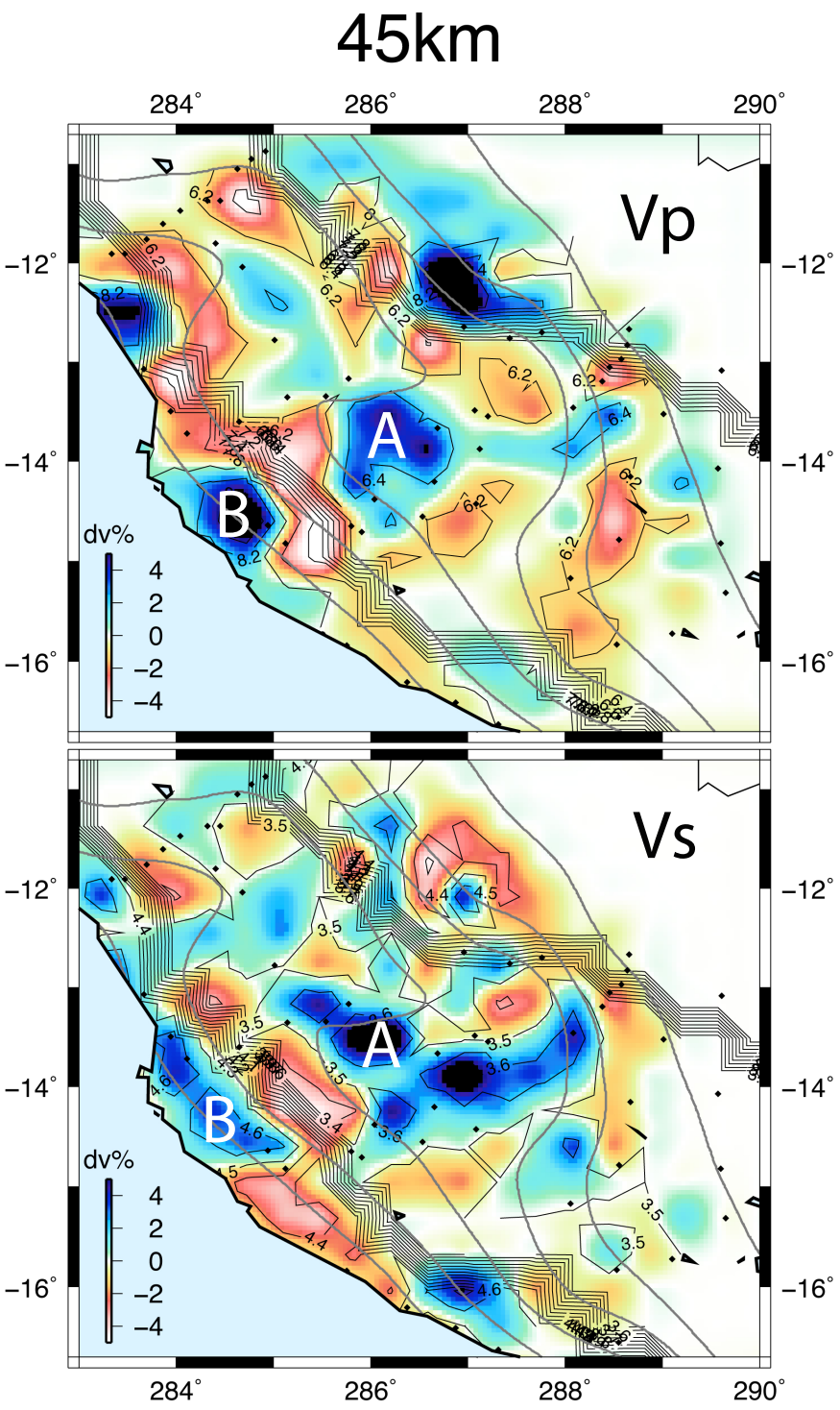

Figure 10: Results of tomographic inversion at 45 km depth after 4 iterations, with damping parameter (α) equal to 35. Anomalies A and B are labeled. Black lines indicate absolute velocity contours according to deviations. The multiple close contours show the location of the Moho. Gray lines show the slab contours of Hayes et al. [2012].

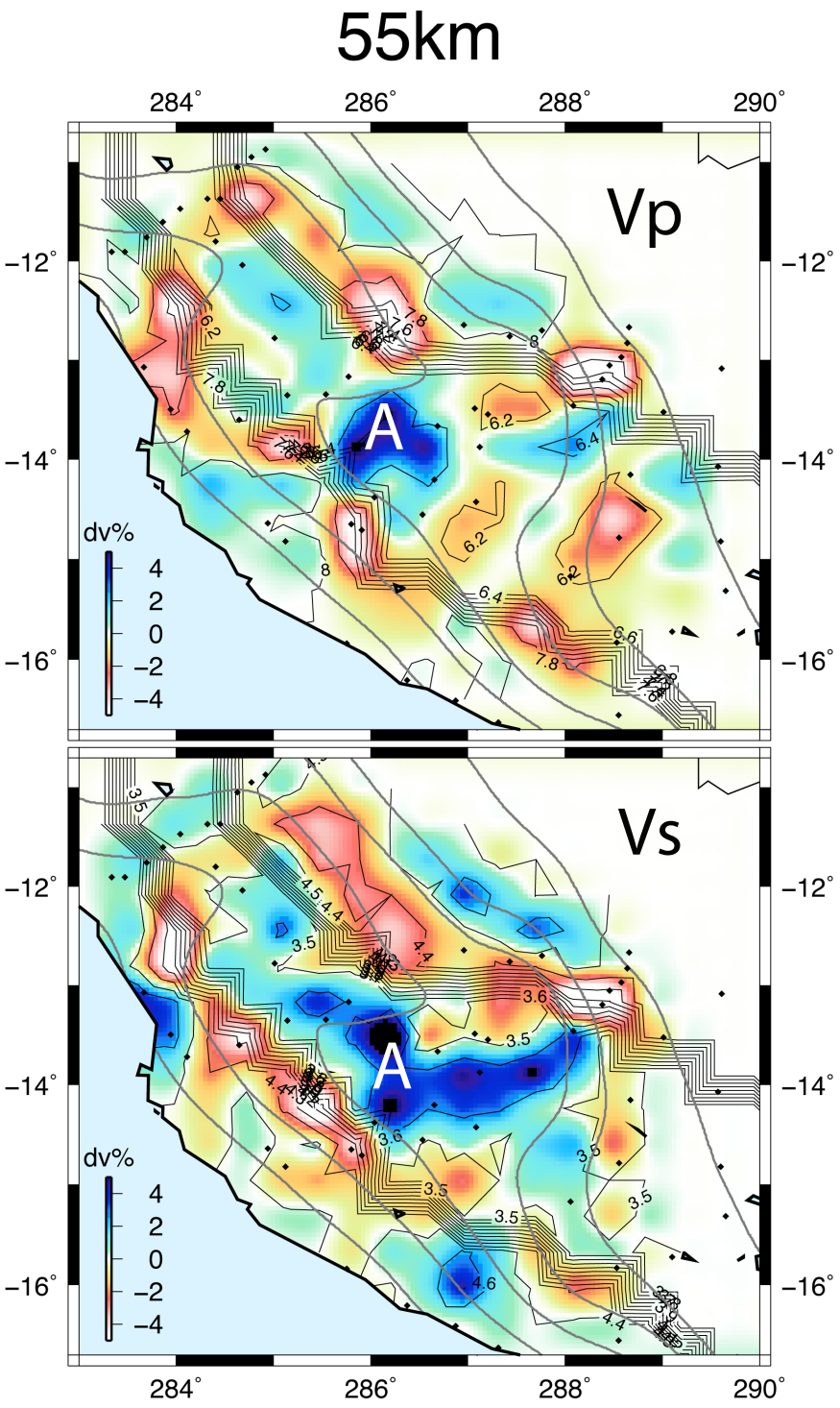

Figure 11: Results of tomographic inversion at 55 km depth after 4 iterations, with damping parameter (α) equal to 35.Black lines indicate absolute velocity contours according to deviations. The multiple close contours show the location of the Moho. Gray lines show the slab contours of Hayes et al. [2012].

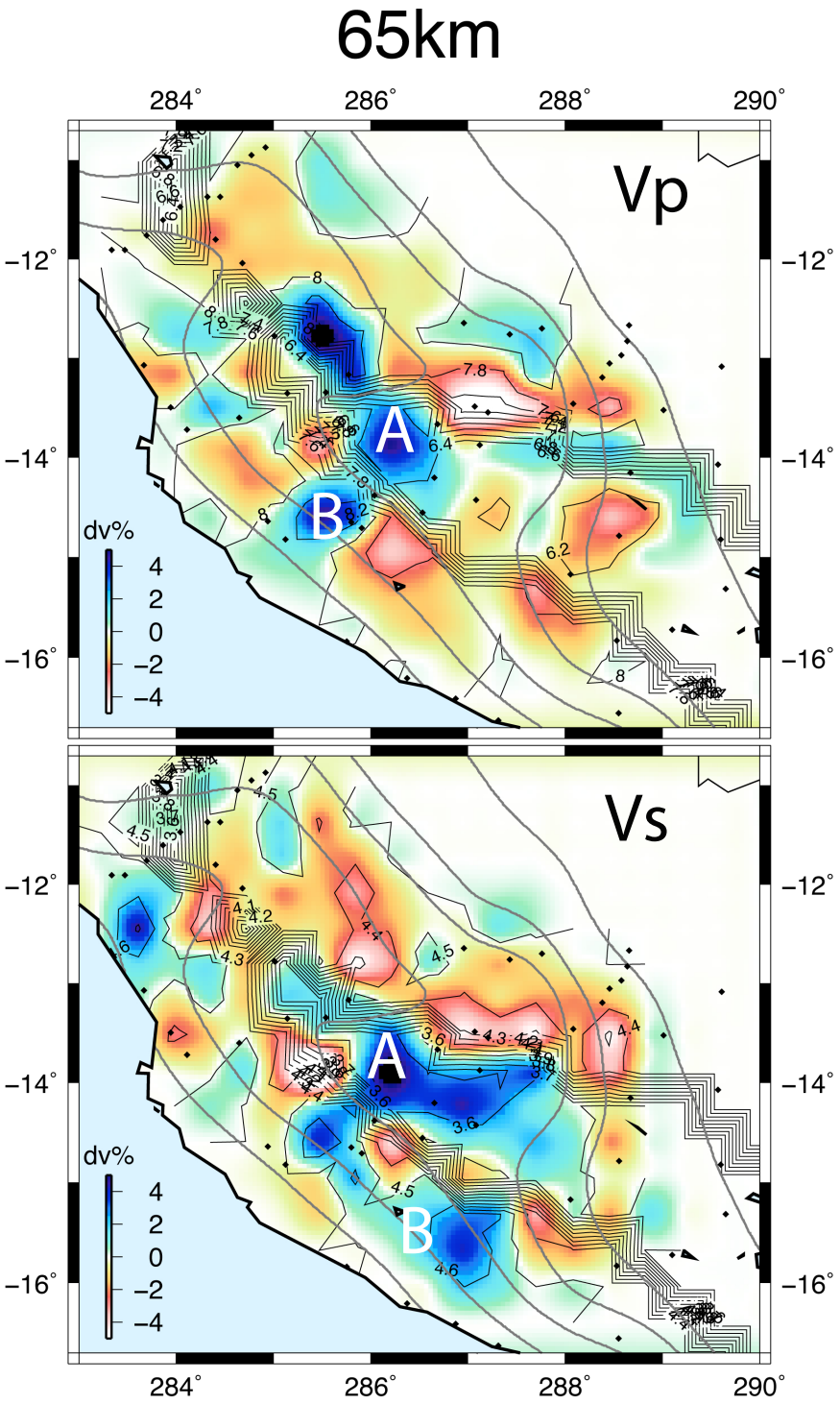

Figure 12: Results of tomographic inversion at 65 km depth after 4 iterations, with damping parameter (α) equal to 35. Black lines indicate absolute velocity contours according to deviations. The multiple close contours show the location of the Moho. Gray lines show the slab contours of Hayes et al. [2012].

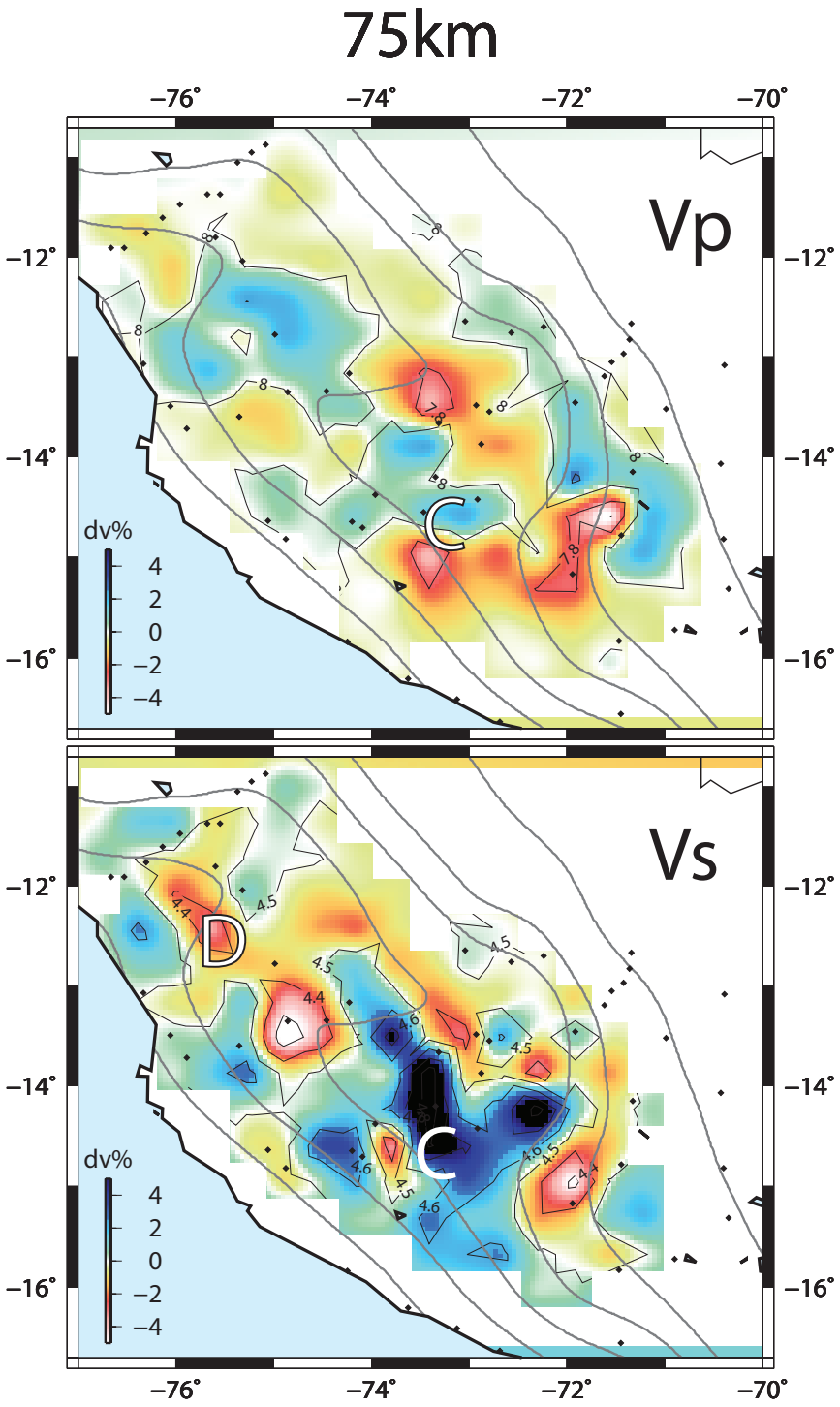

Figure 13: Results of tomographic inversion at 75 km depth after 4 iterations, withdamping parameter (α) equal to 35. Black lines indicate absolute velocity contours according to deviations. The multiple close contours show the location of the Moho. Gray lines show the slab contours of Hayes et al. [2012].

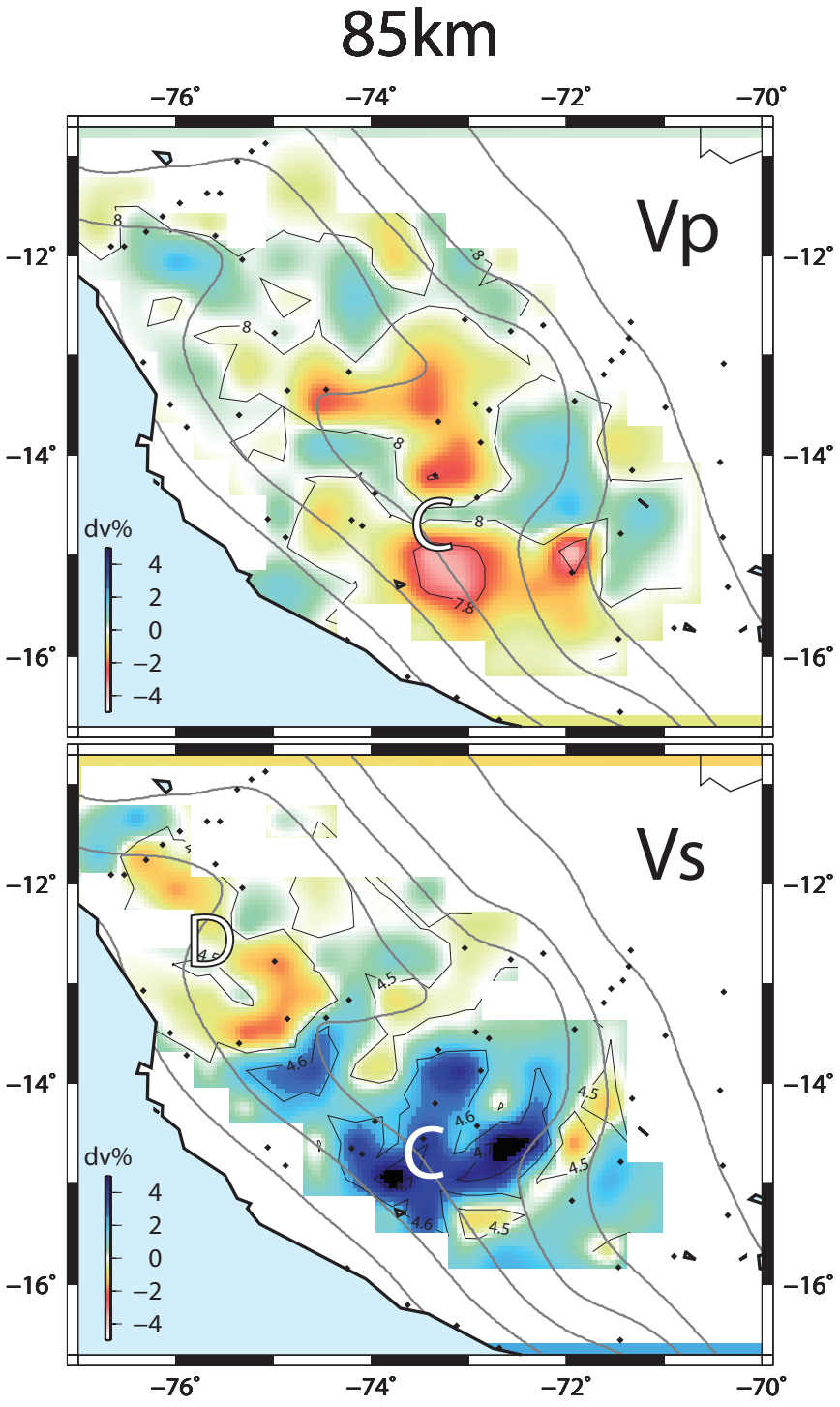

Figure 14: Results of tomographic inversionat 85 km depth after 4 iterations, with damping parameter (α) equal to 35. Black lines indicate absolute velocity contours according to deviations. The multiple close contours show the location of the Moho. Gray lines show the slab contours of Hayes et al. [2012].

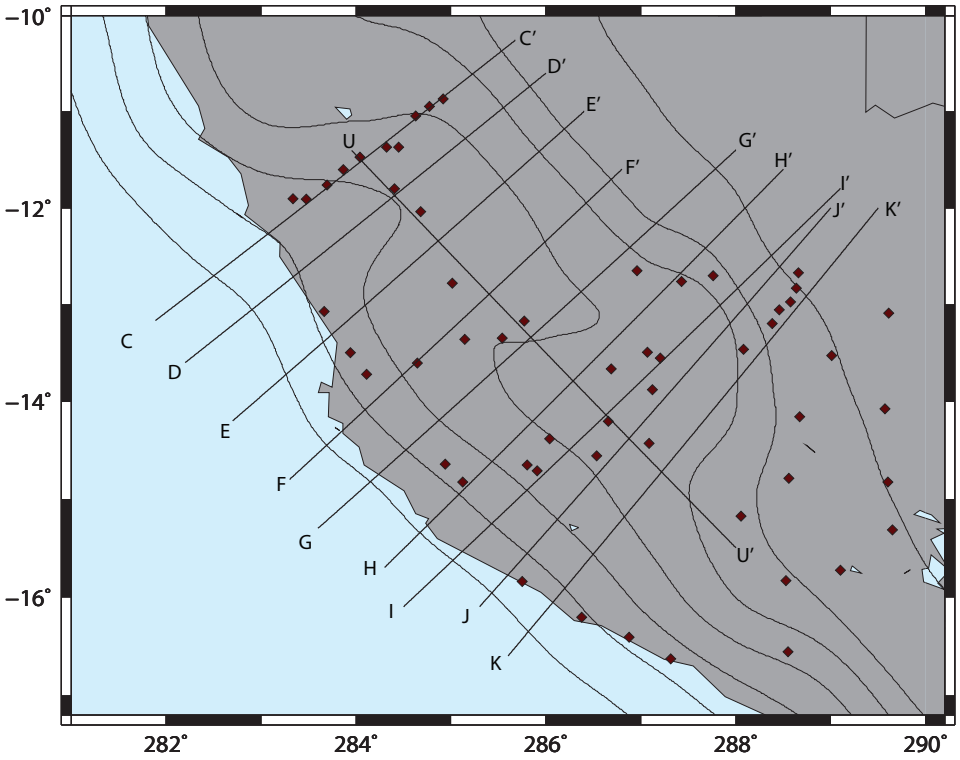

Figure 15: Map showings locations for the cross-sections shown in Figures 16-25.

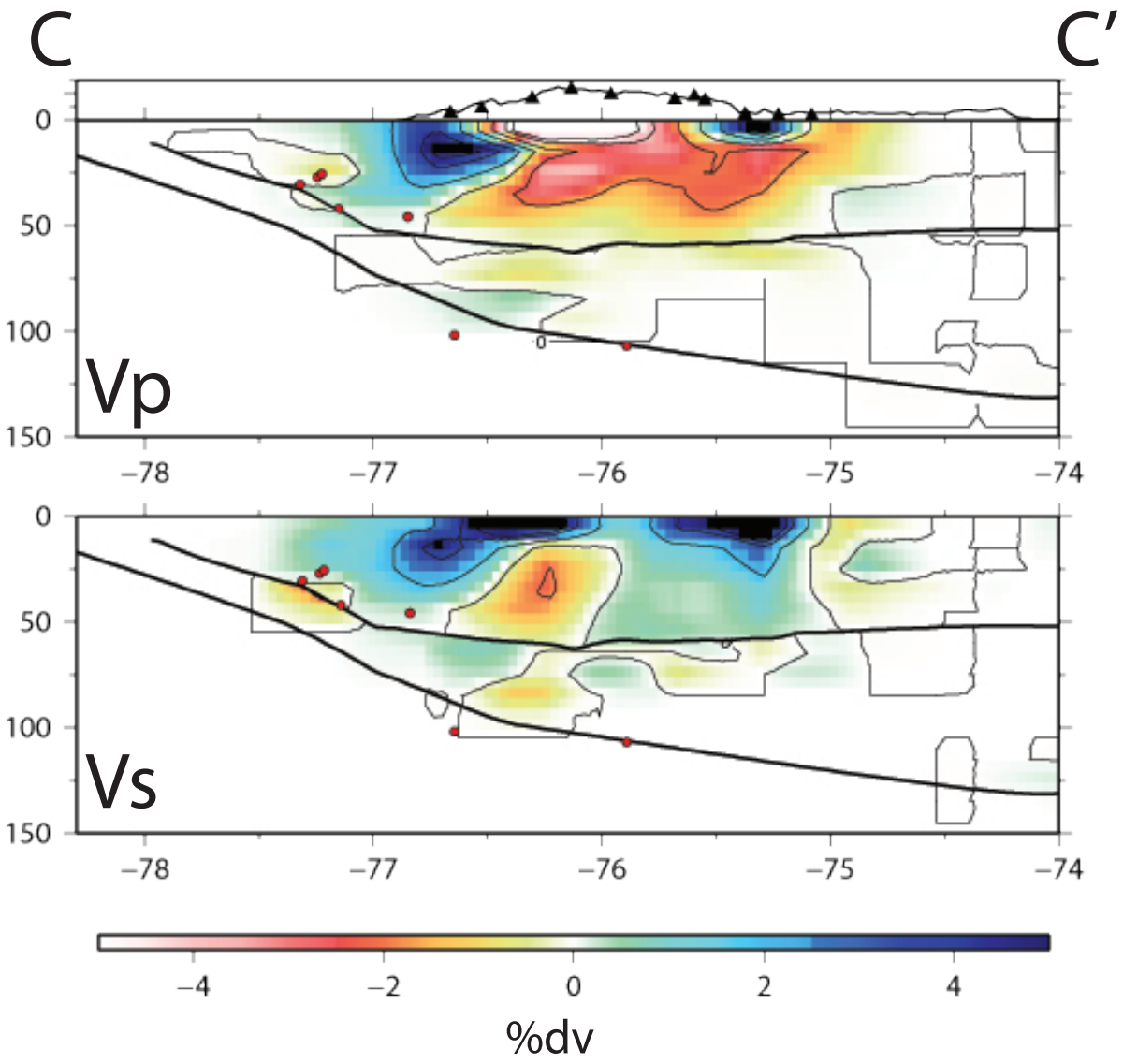

Figure 16: Cross-section C-C', located beneath the northern transect of stations

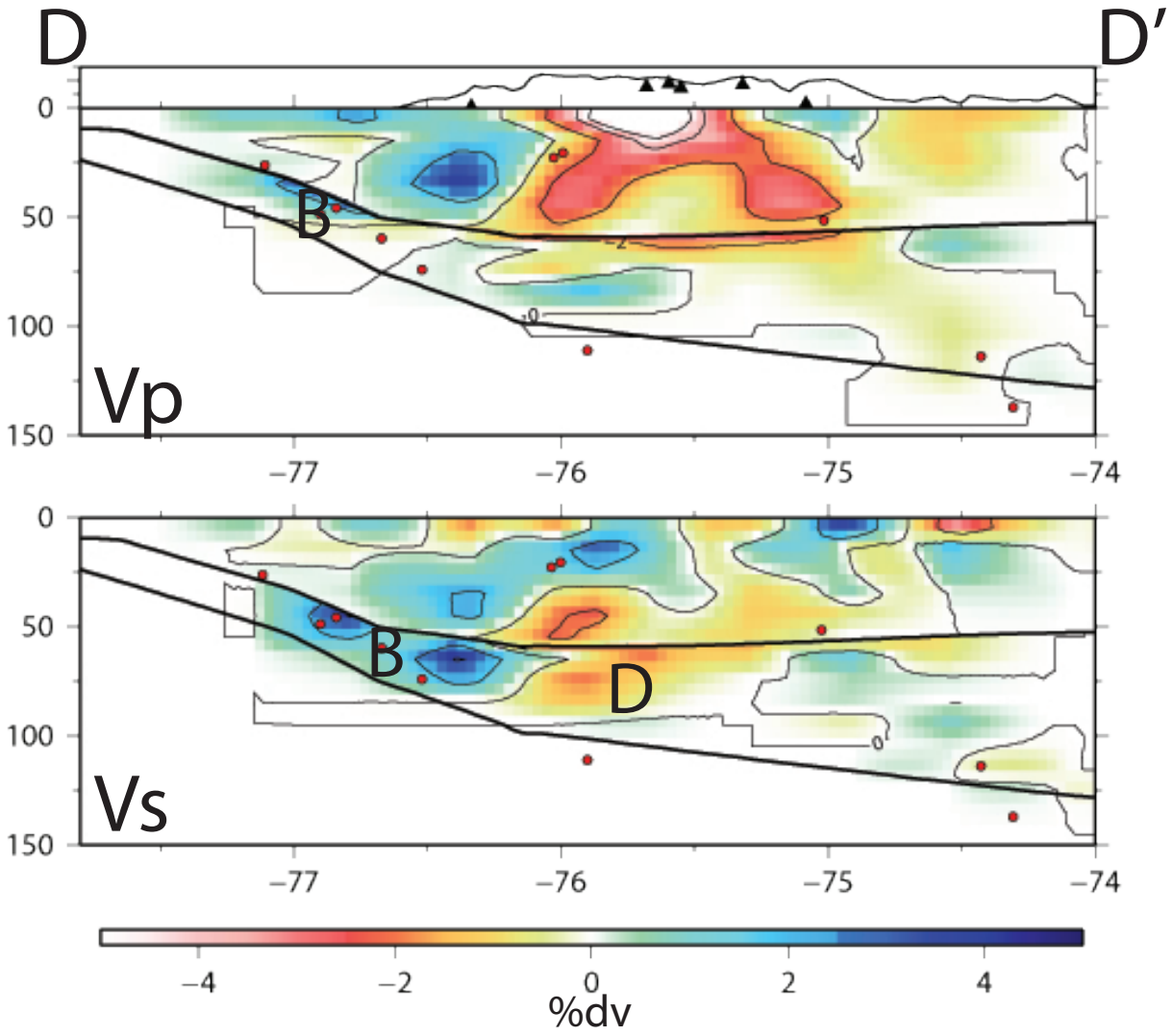

Figure 17: Cross-section D-D’

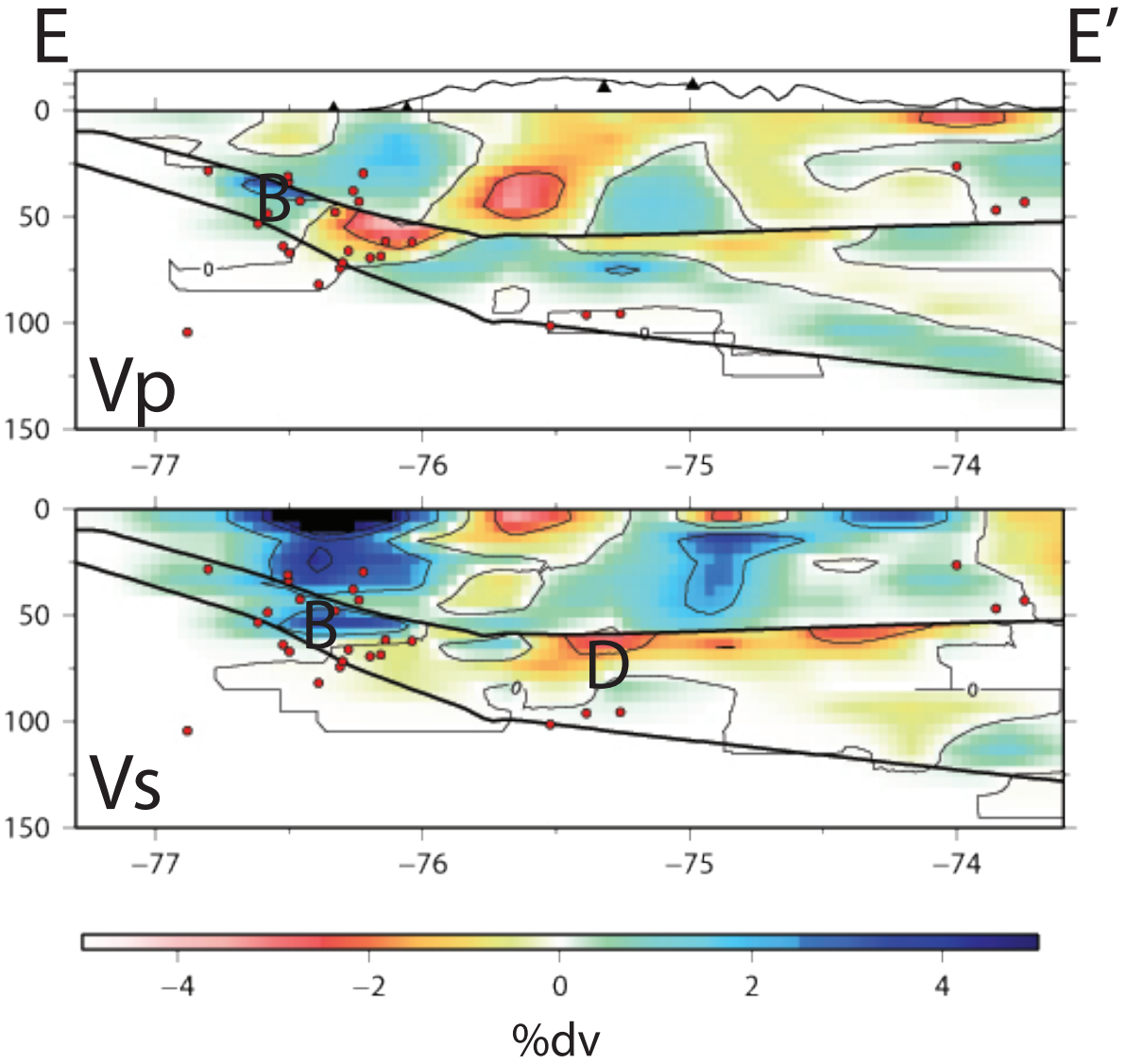

Figure 18: Cross-section E-E’

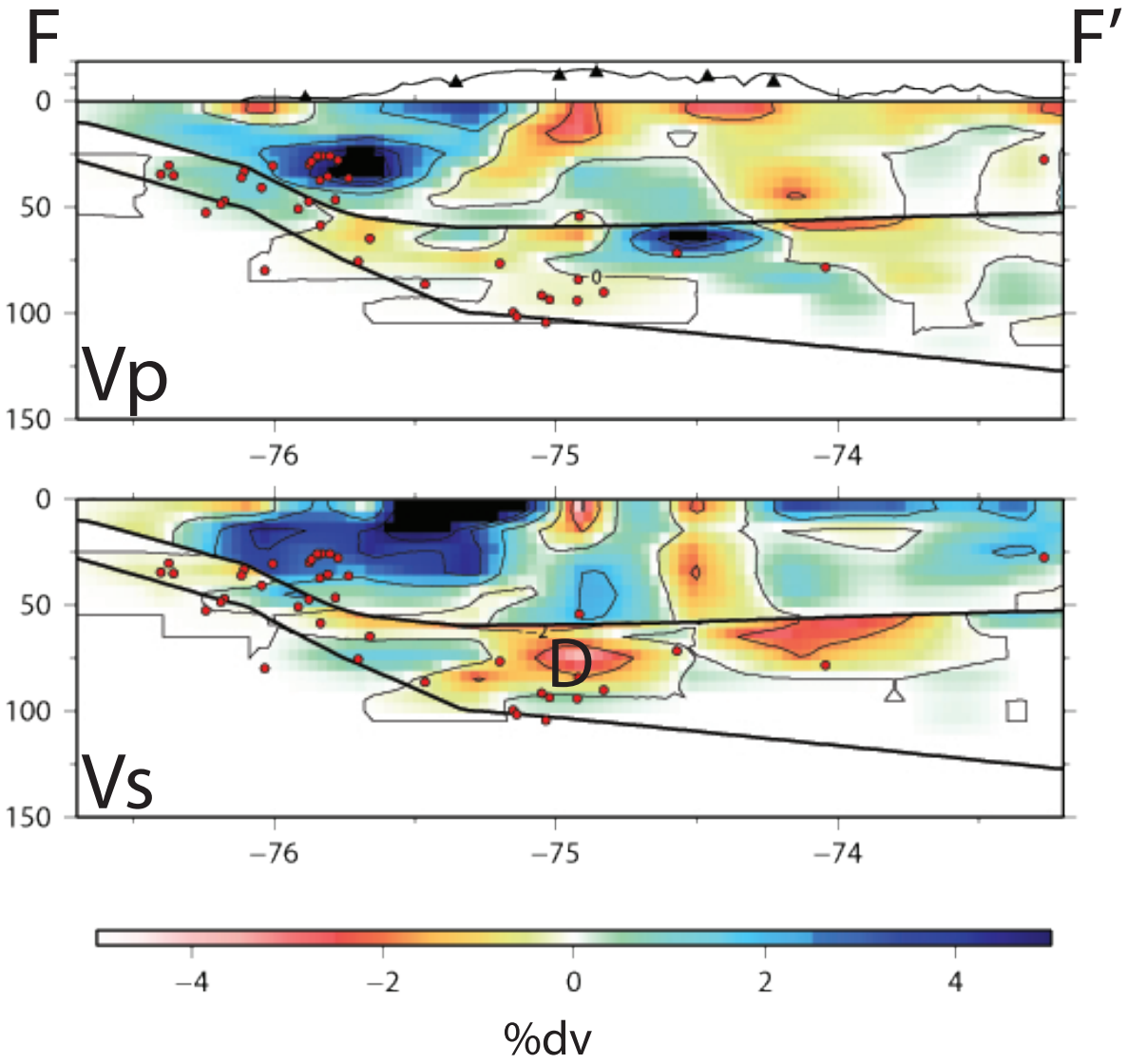

Figure 19: Cross-section F-F'

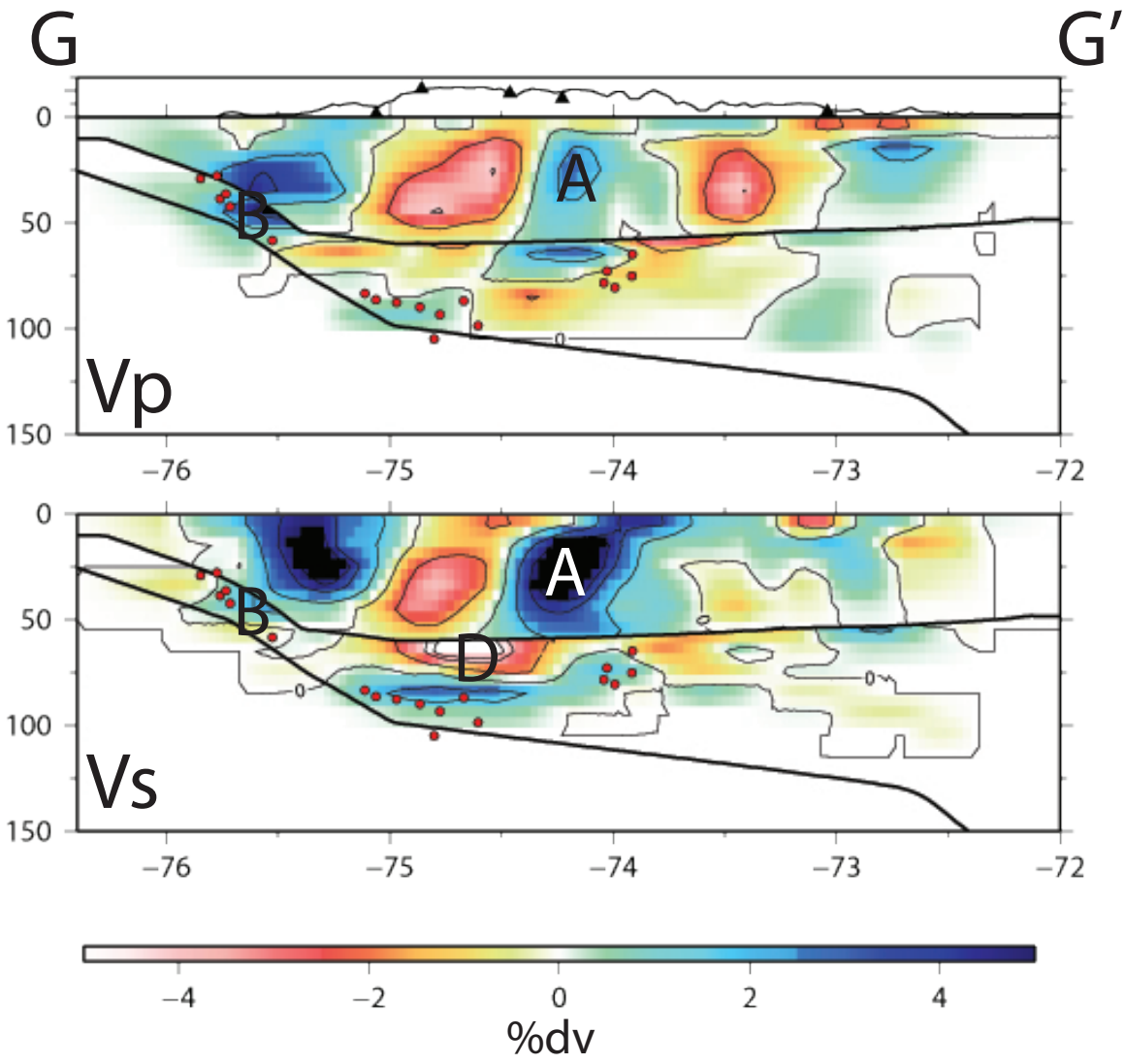

Figure 20: Cross-section G-G'

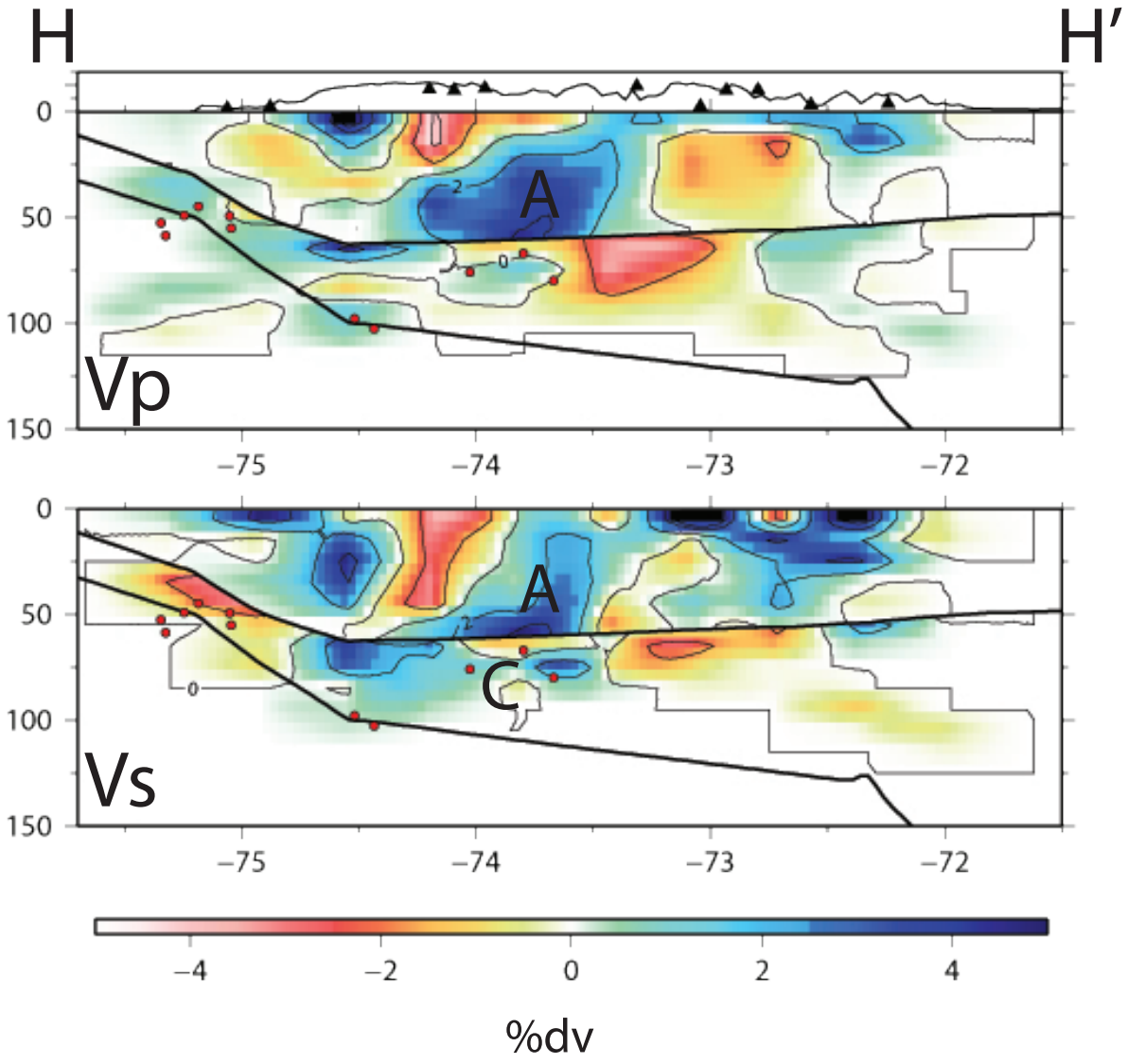

Figure 21: Cross-section H-H’

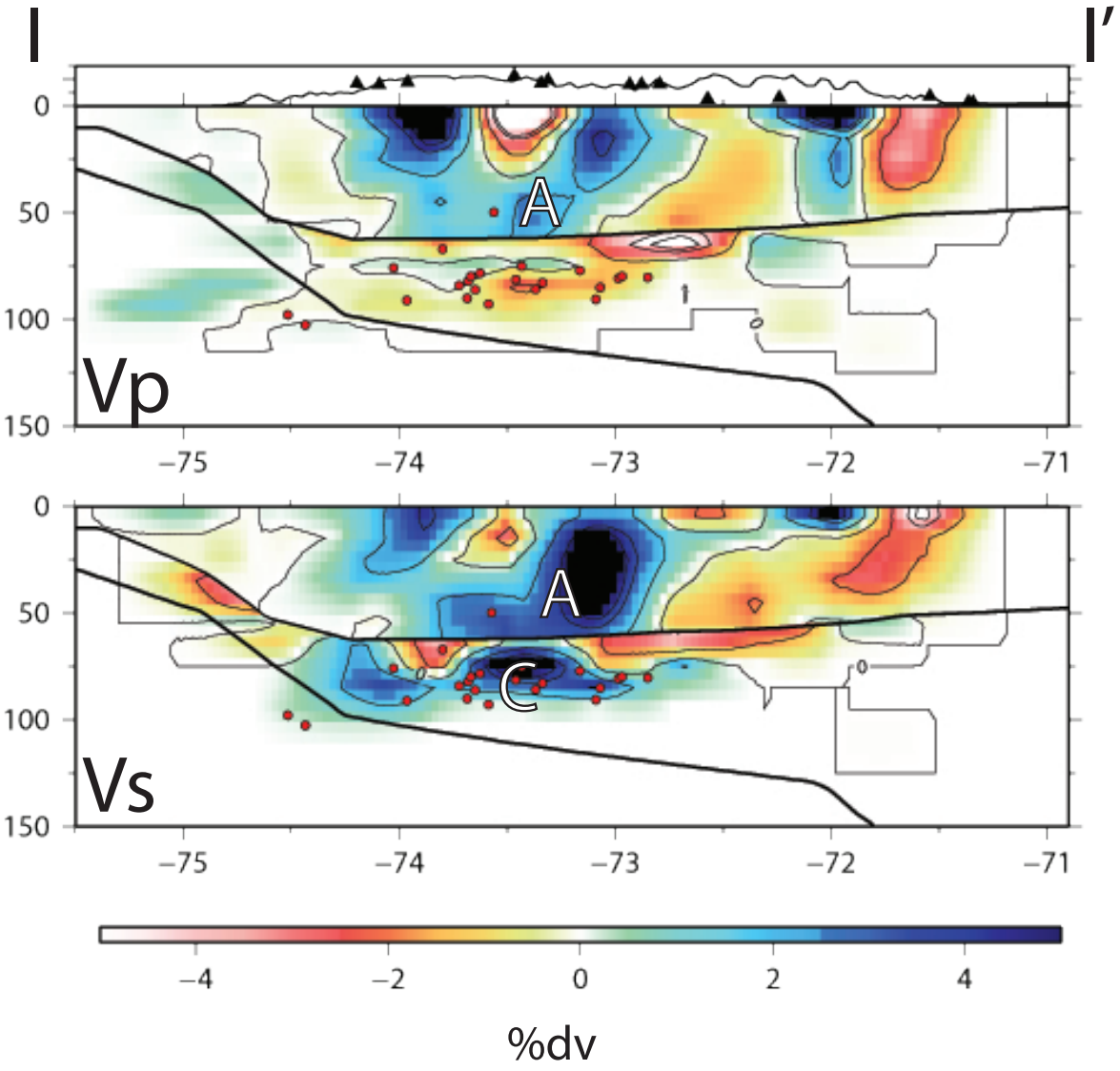

Figure 22: Cross-section I-I'

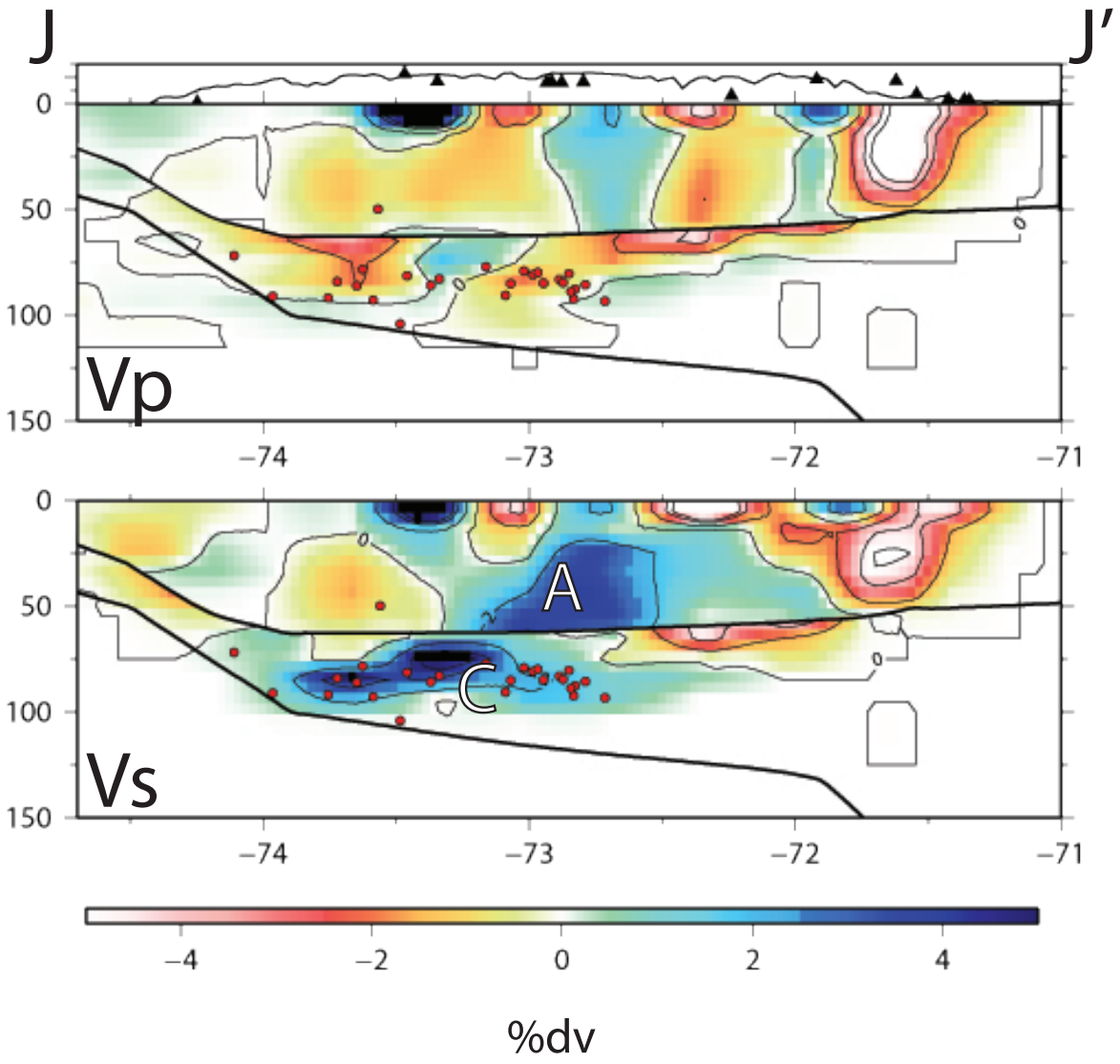

Figure 23: Cross-section J-J'

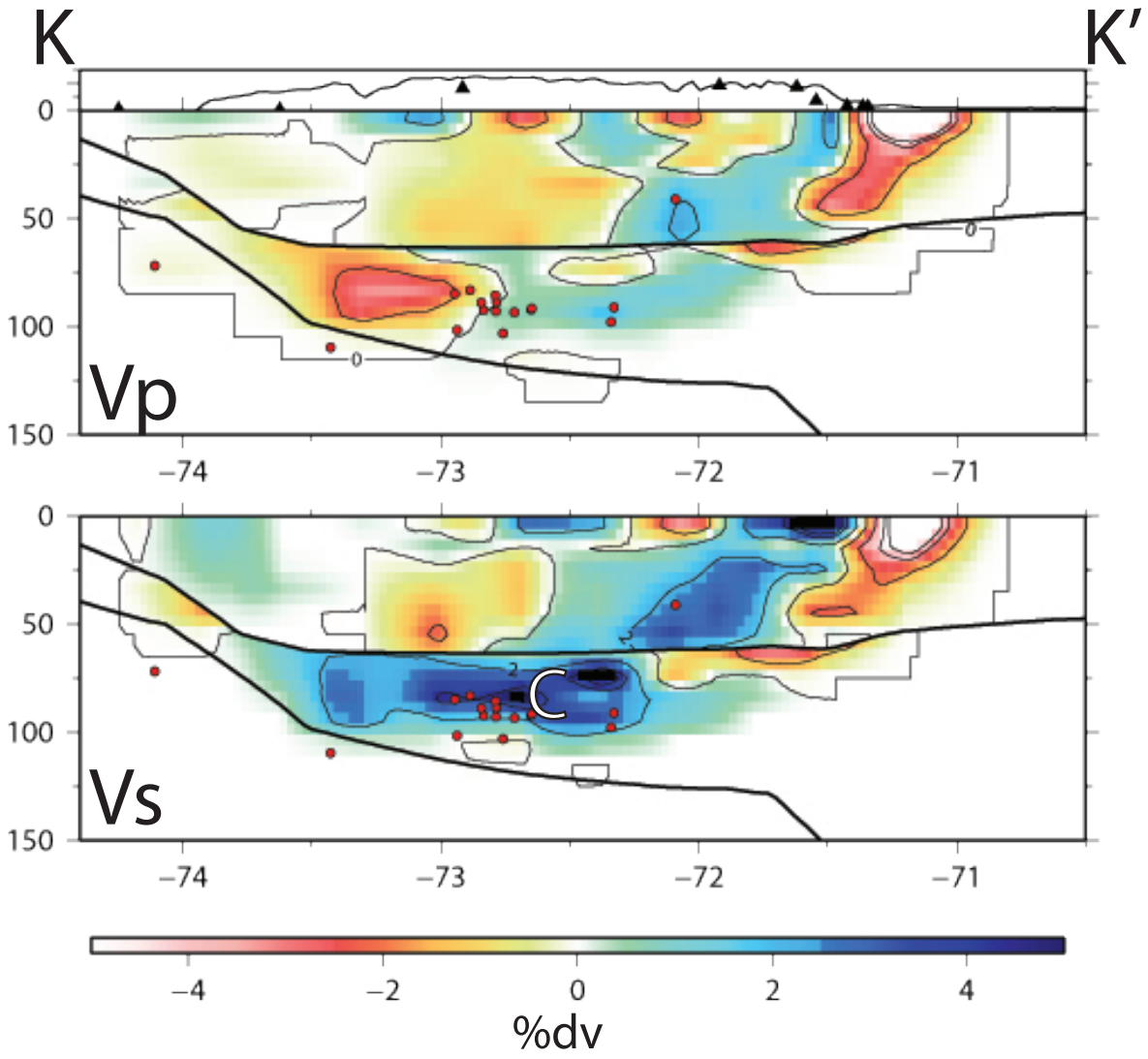

Figure 24: Cross-section K-K’

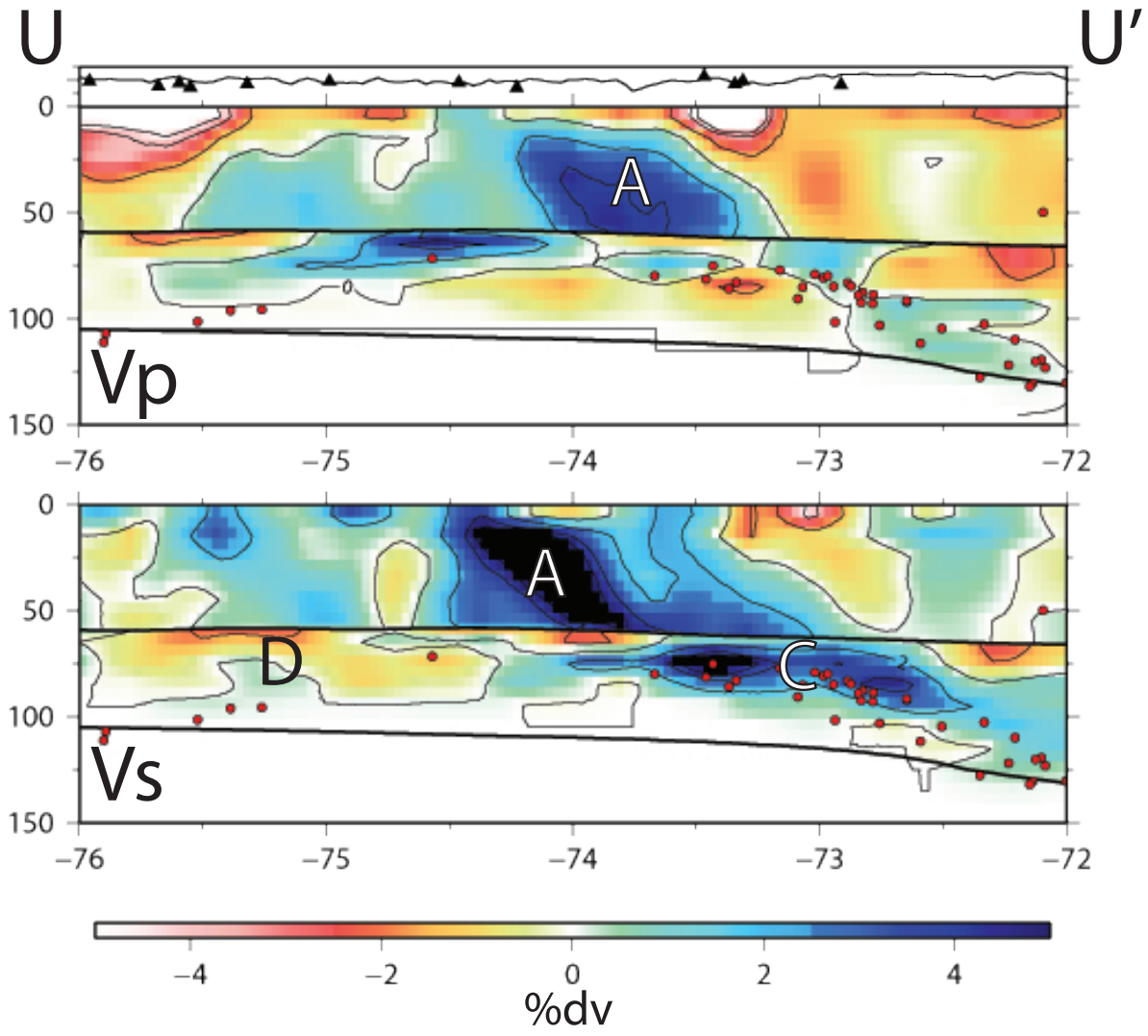

Figure 25: Cross-section U-U’, oriented roughly parallel to the trench

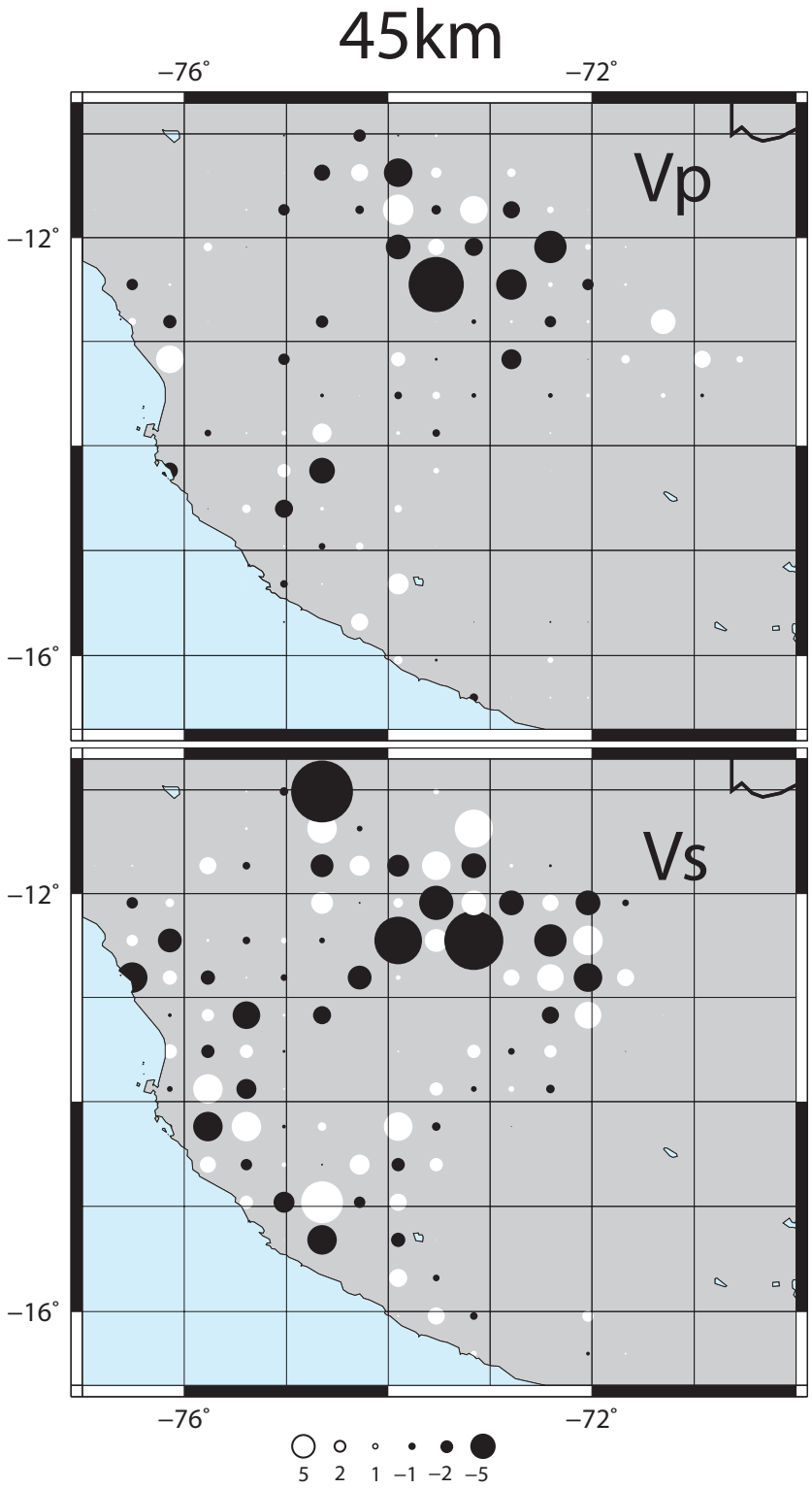

Figure 26: Results showing the recovery of checkerboard at 45 km.

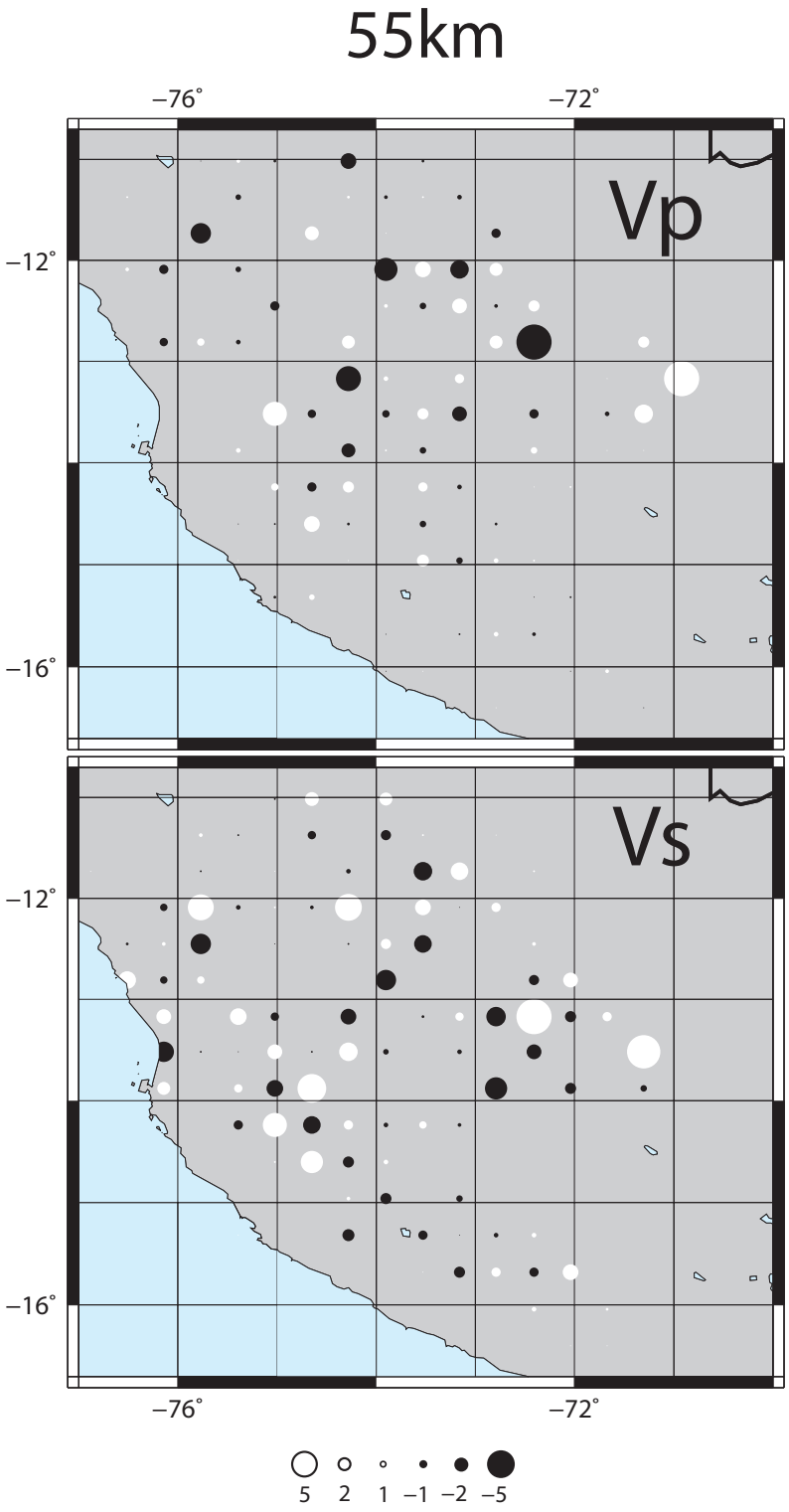

Figure 27: Results showing the recovery of checkerboard at 55 km.

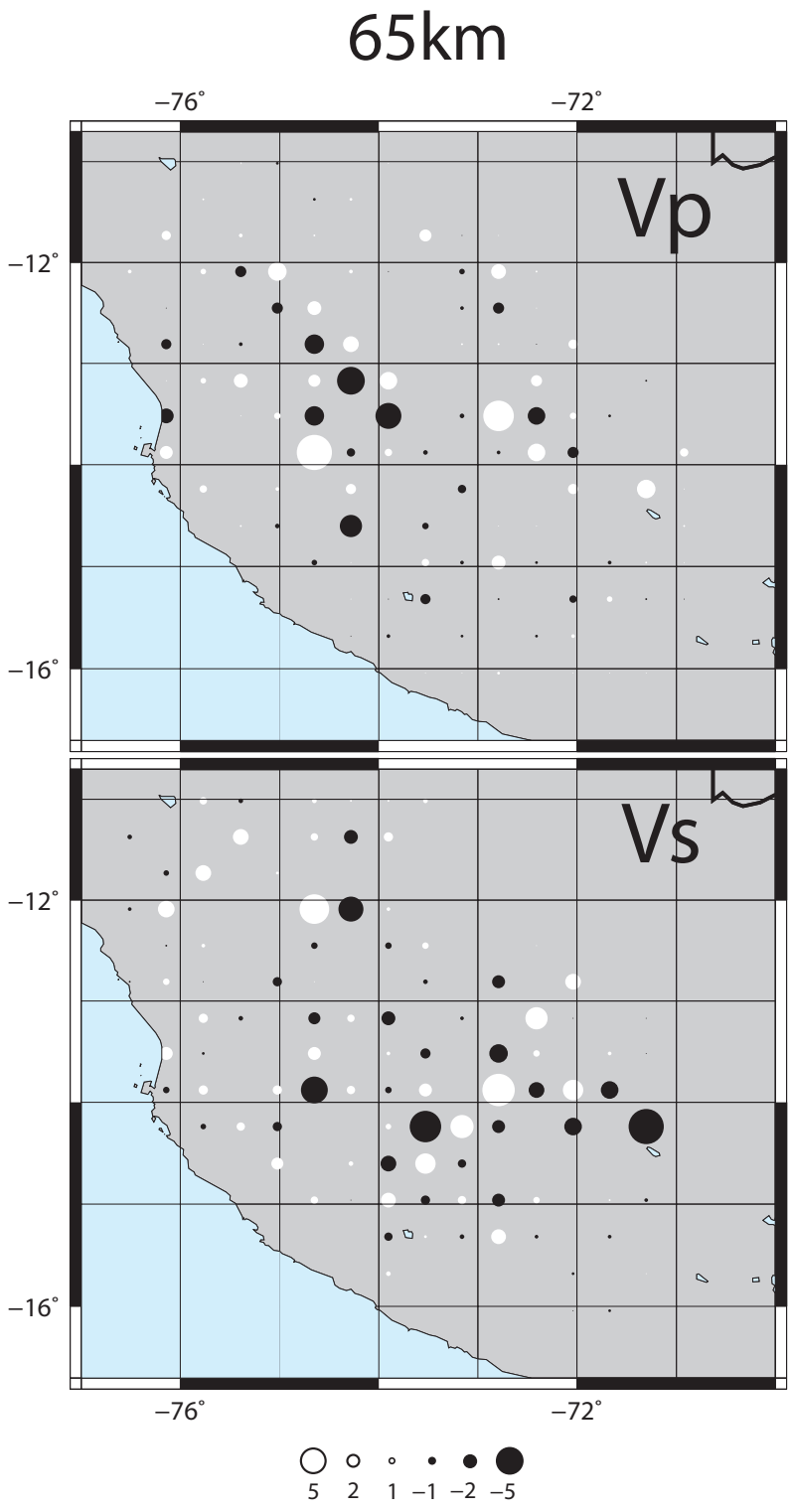

Figure 28: Results showing the recovery of checkerboard at 65 km.

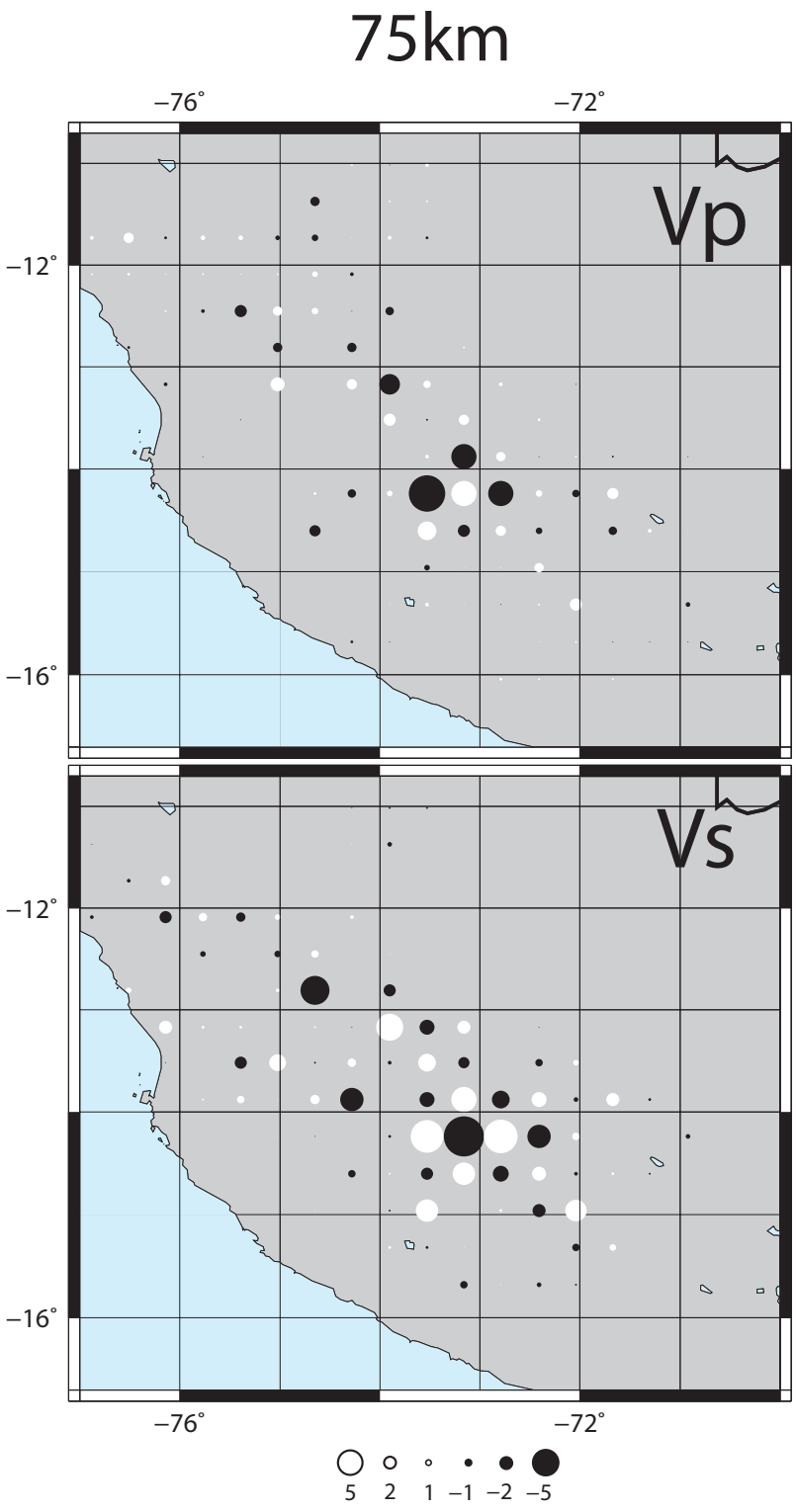

Figure 29: Results showing the recovery of checkerboard at 75 km.

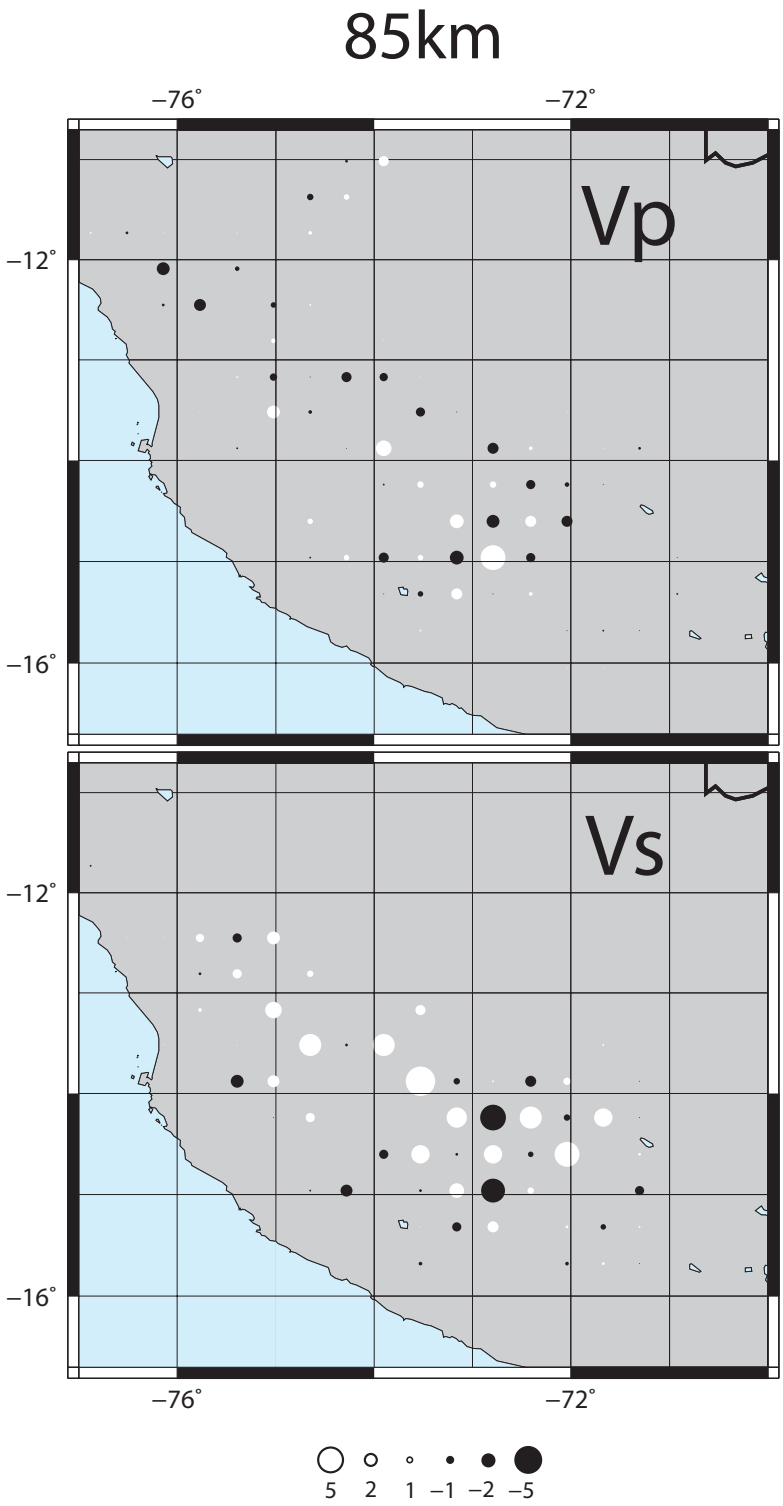

Figure 30: Results showing the recovery of checkerboard at 85 km.

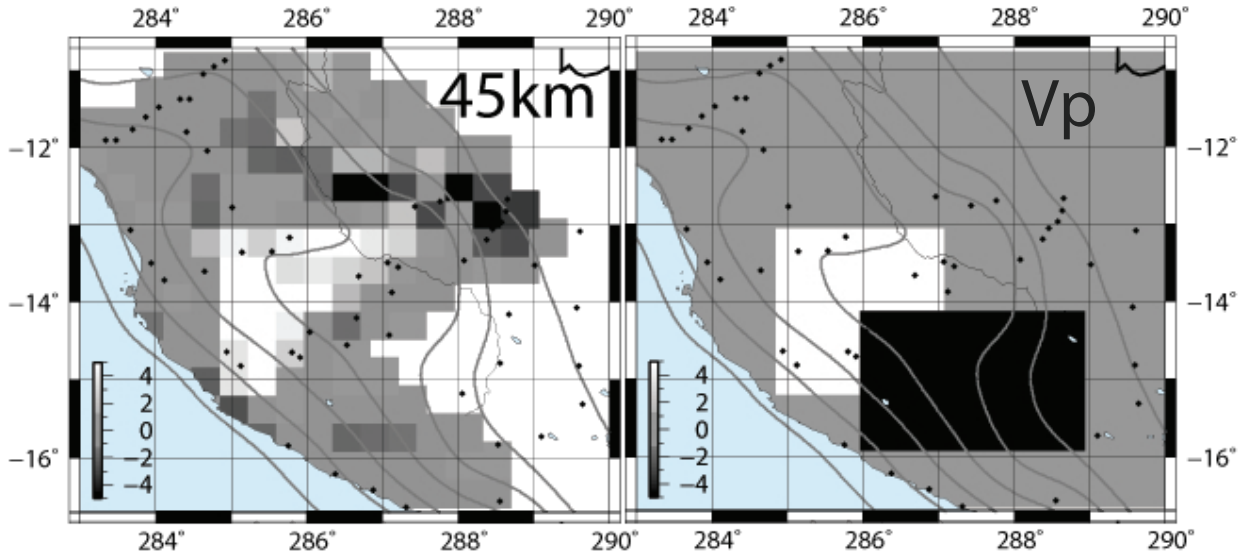

Figure 31: Results showing recovery of anomaly A at 45 km in Vp.

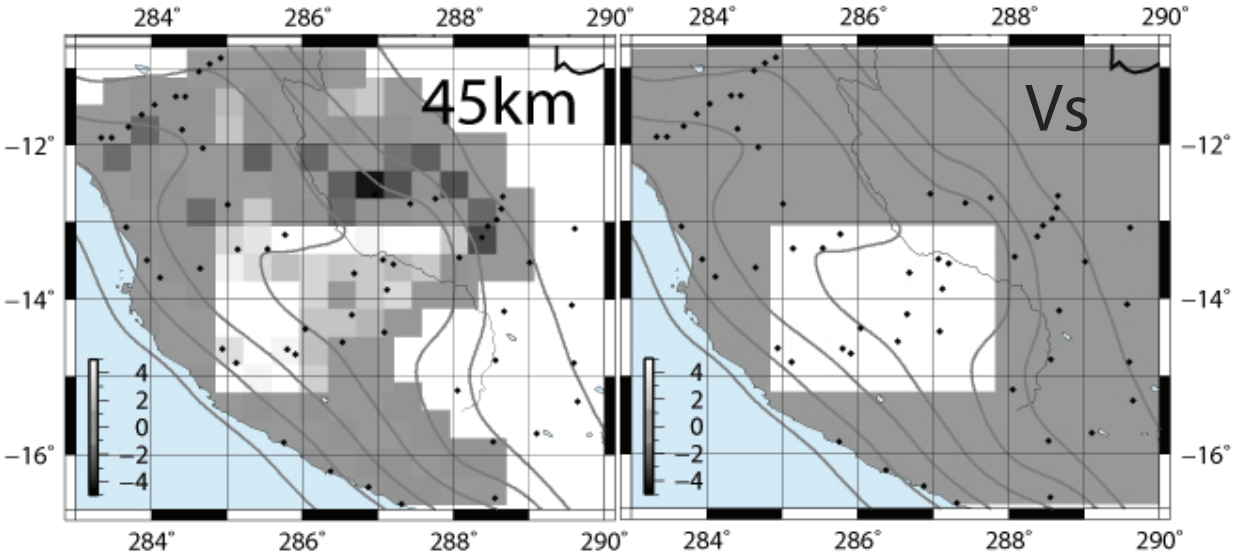

Figure 32: Results showing recovery of anomaly A at 45 km in Vs.

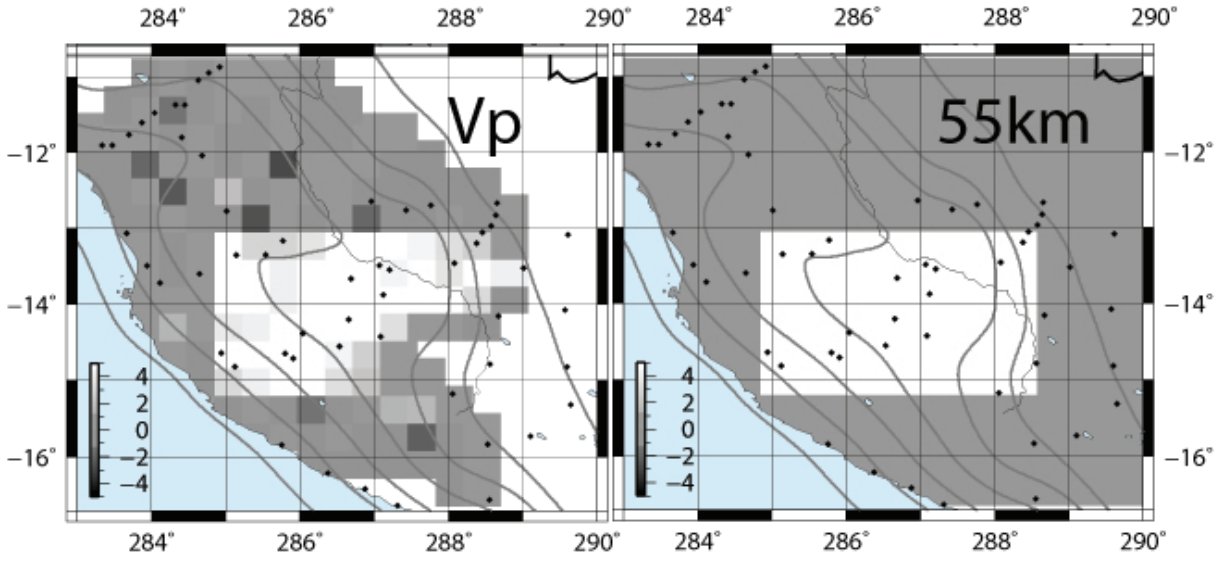

Figure 33: Results showing recovery of anomaly A at 55 km in Vp.

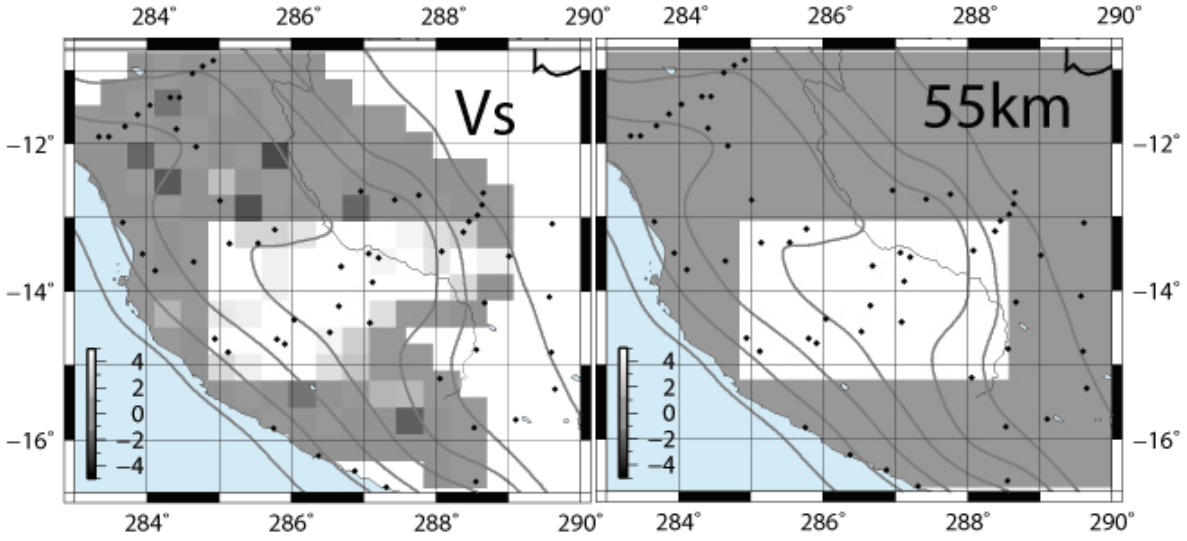

Figure 34: Results showing recovery of anomaly A at 55 km in Vs.

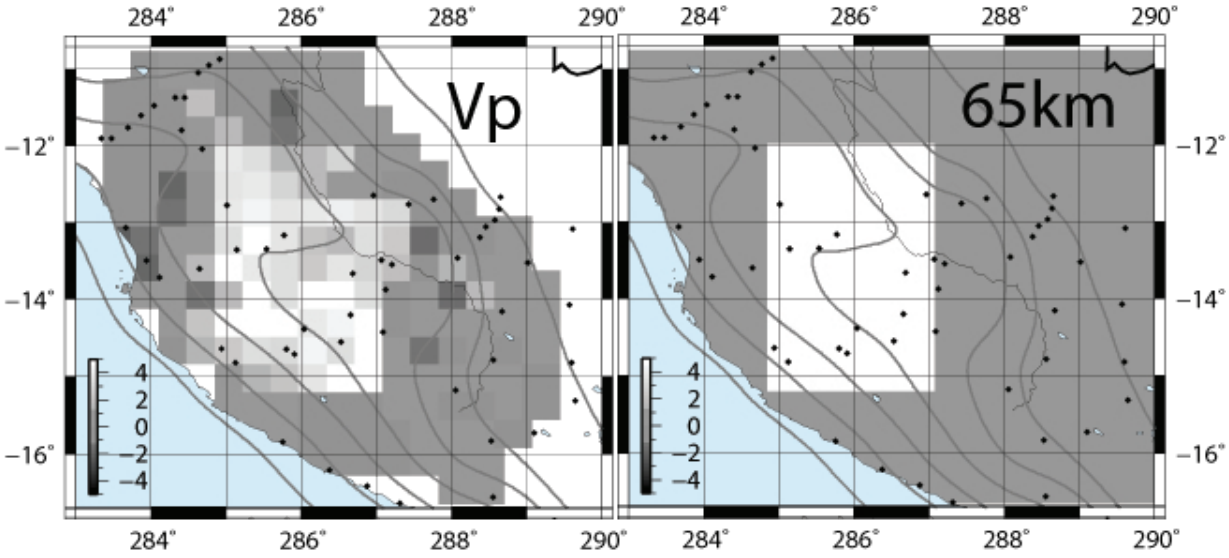

Figure 35: Results showing recovery of anomaly A at 65 km in Vp.

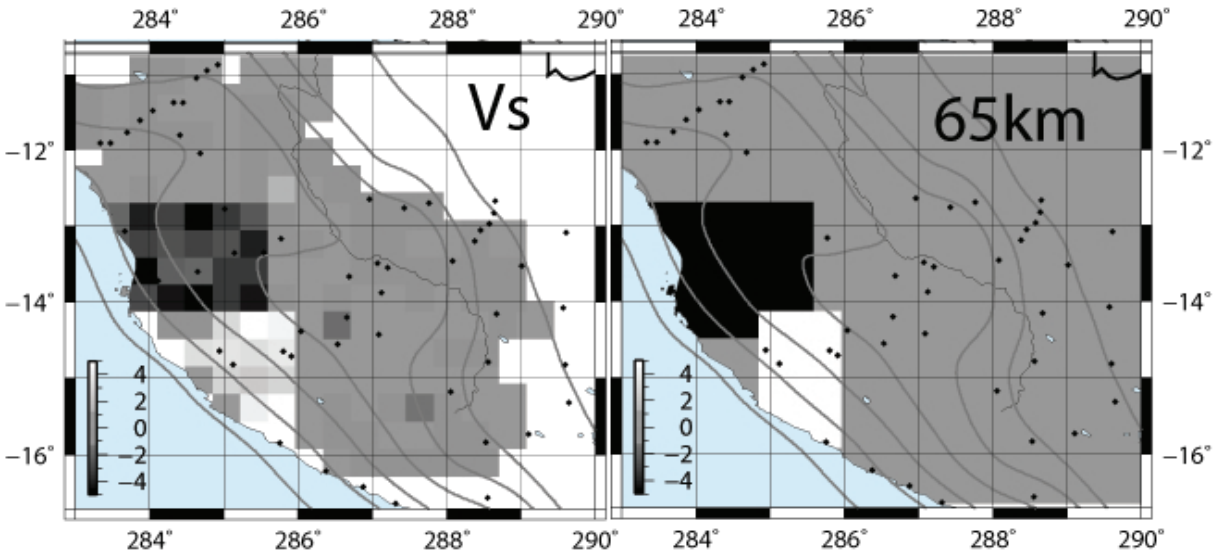

Figure 36: Results showing recovery of anomaly A at 65 km in Vs.

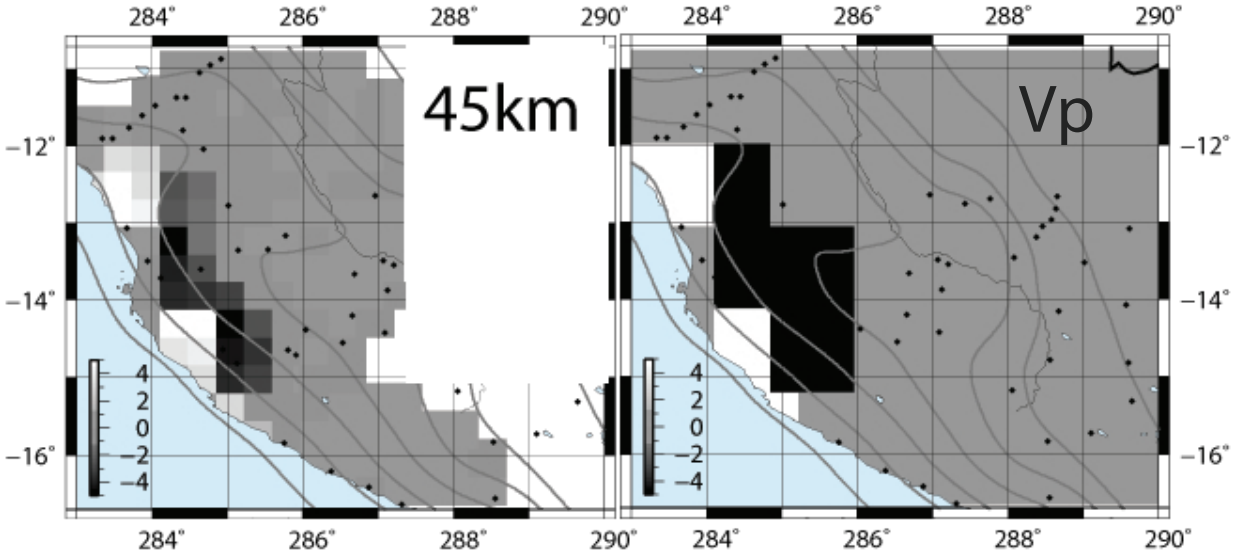

Figure 37: Results showing recovery of anomaly B at 45 km in Vp.

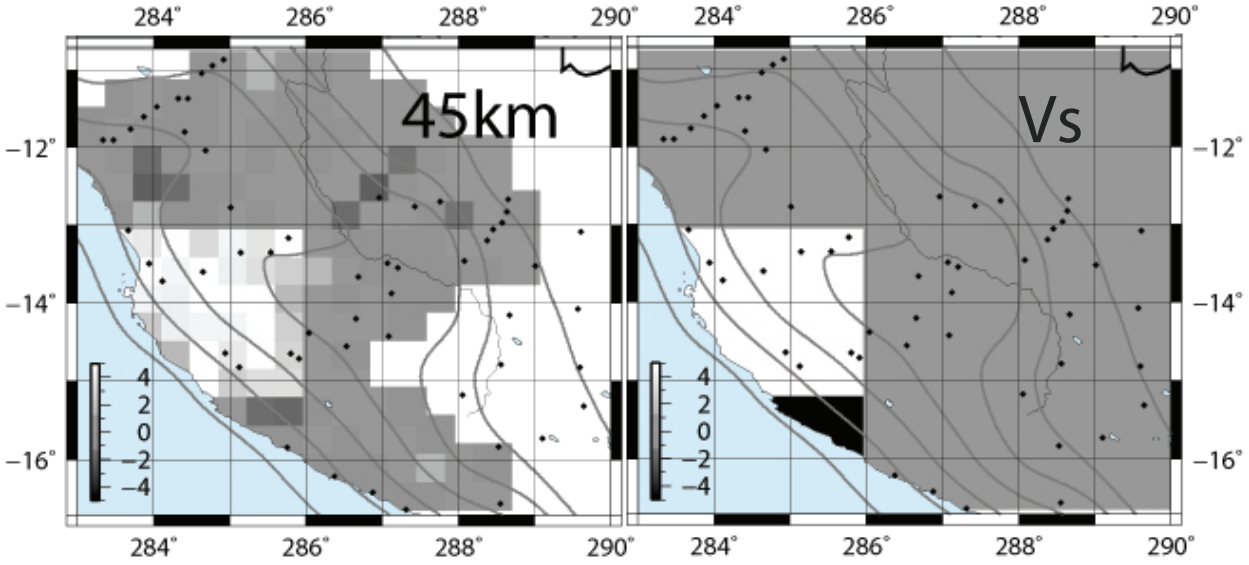

Figure 38: Results showing recovery of anomaly B at 45 km in Vs.

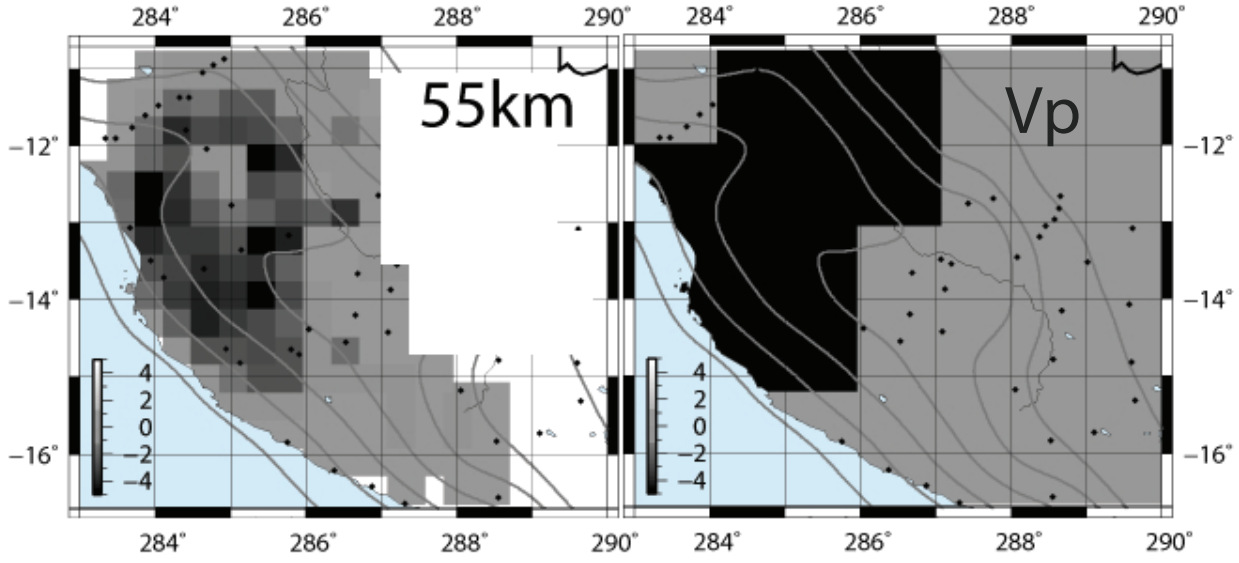

Figure 39: Results showing recovery of anomaly B at 55 km in Vp.

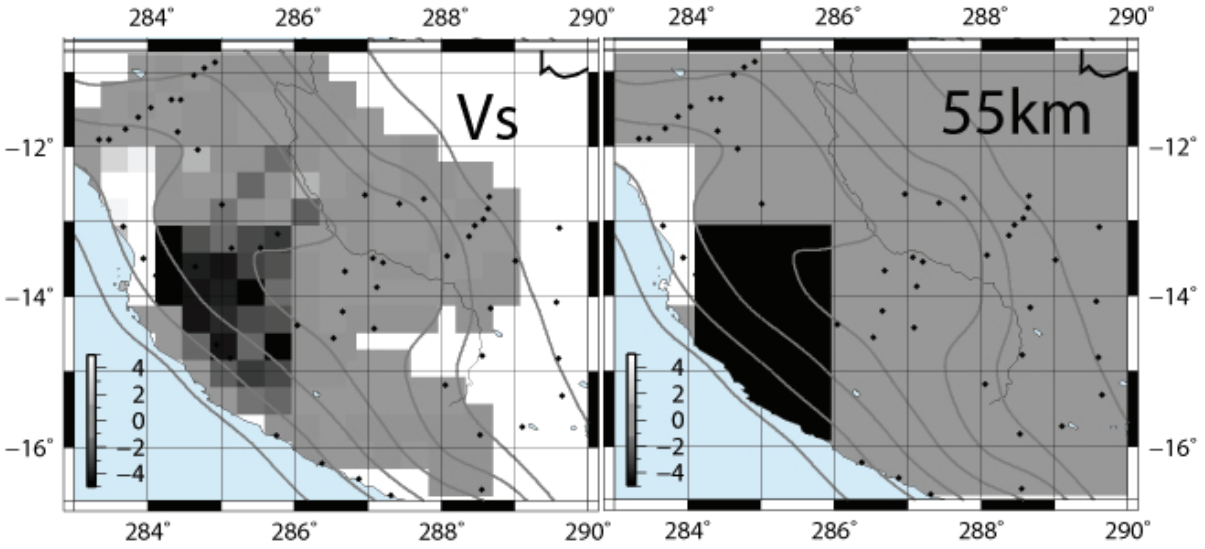

Figure 40: Results showing recovery of anomaly B at 55 km in Vs.

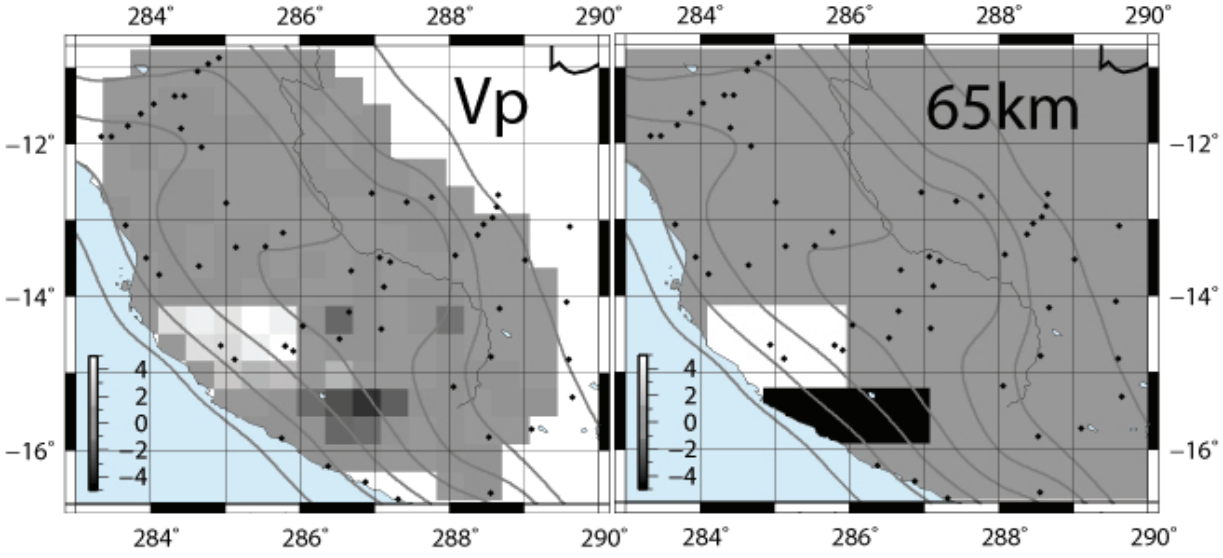

Figure 41: Results showing recovery of anomaly B at 65 km in Vp.

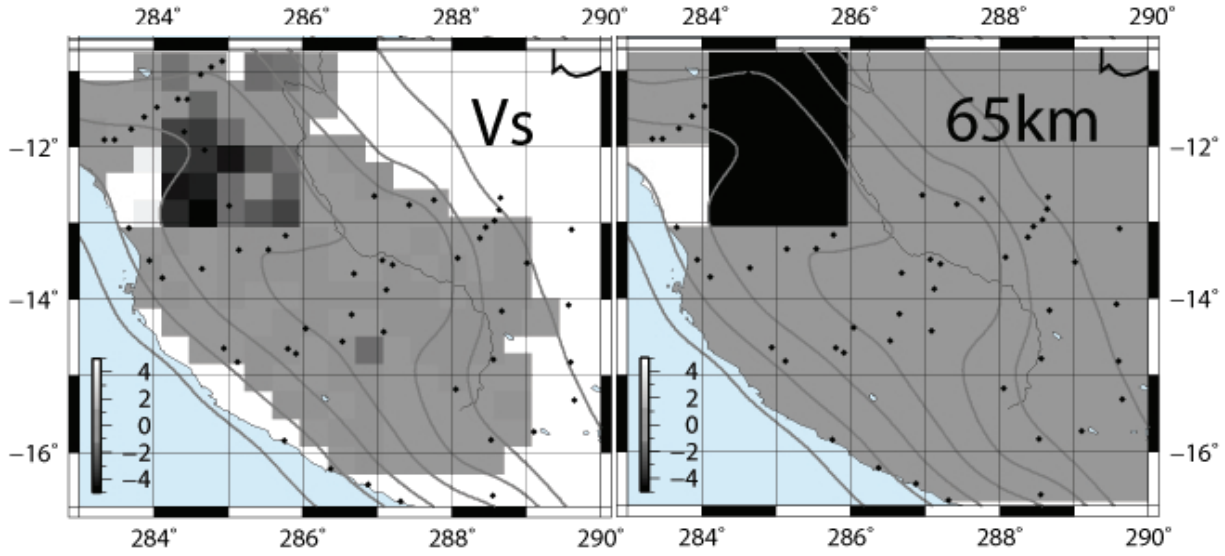

Figure 42: Results showing recovery of anomaly B at 65 km in Vs.

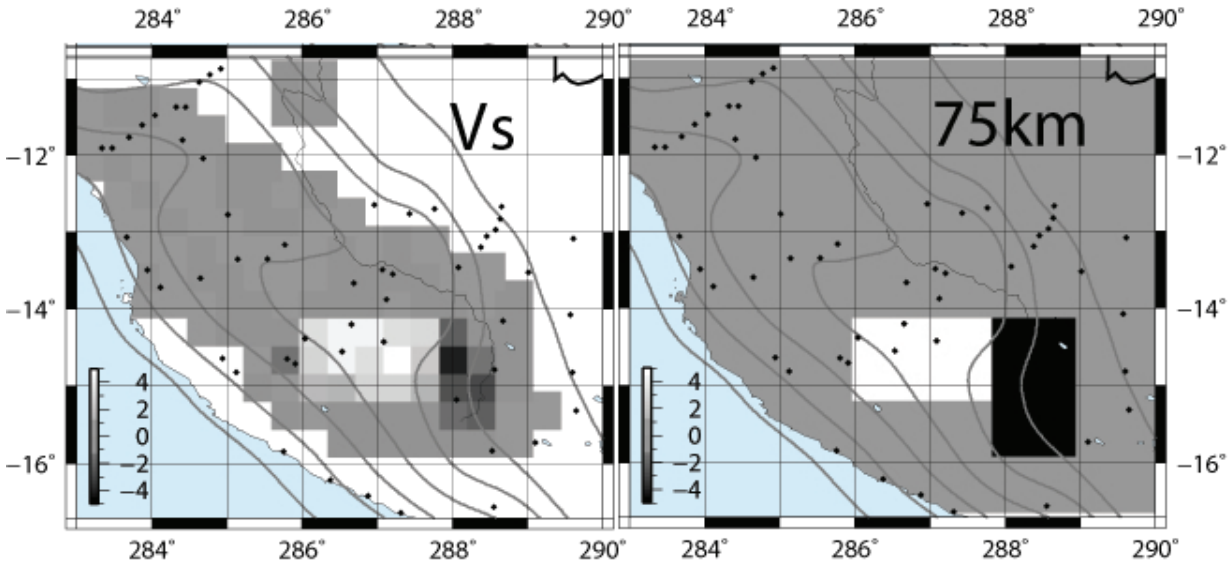

Figure 43: Results showing recovery region near anomaly C at 75 km in Vs.

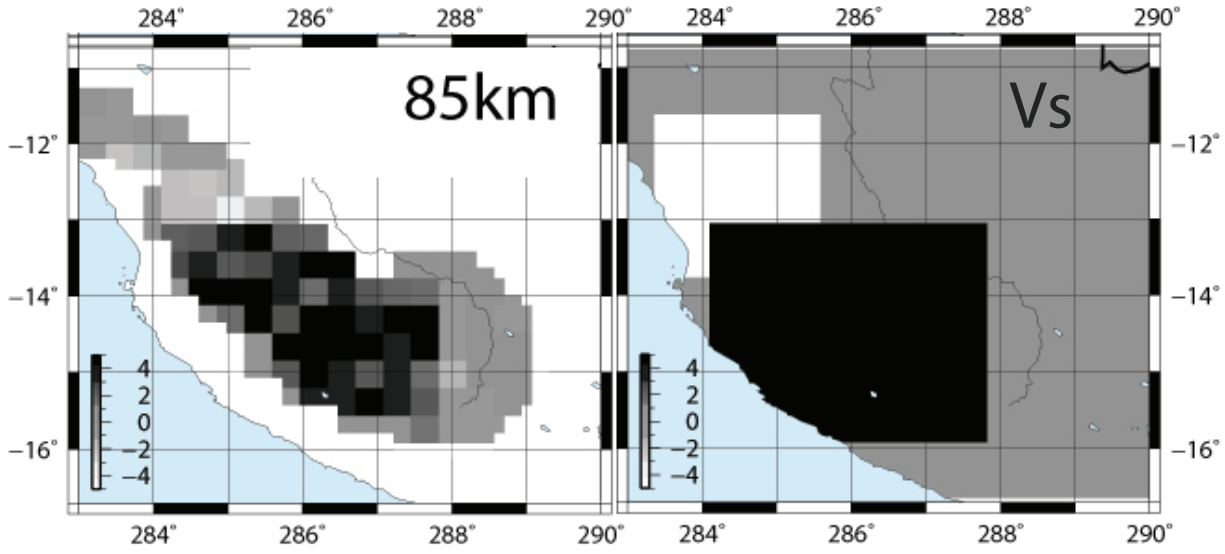

Figure 44: Results showing recovery region near anomaly C at 85 km in Vs.

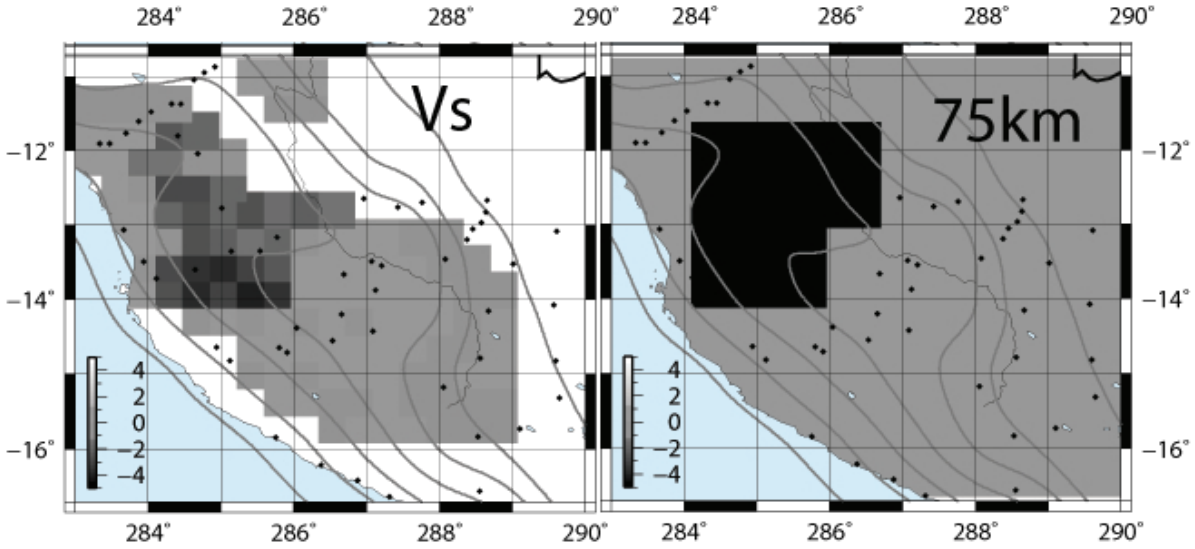

Figure 45: Results showing recovery region near anomaly D at 75 km in Vs.

REFERENCES

Aleman, A. M. The Peruvian flat-slab. *Backbone of the Americas: Patagonia to Alaska. Paper no. 1-13. Presented at GSA Speciality Meeting No. 2, p. 21. April 3-7, 2006.*

Barazangi, M. and B. L. Isacks. Spatial distribution of earthquakes and subduction of the Nazca plate beneath South America. *Geology*, 4(11):686–692, 1976.

Bird, P. Laramide crustal thickening event in the Rocky Mountain foreland and Great Plains. *Tectonics*, 3(7):741–758, 1984.

Bird, P. An updated digital model of plate boundaries. *Geochemistry, Geophysics, Geosystems*, 4(3), 2003. doi: 10.1029/2001GC000252.

Cahill, T. A. and B. L. Isacks. Seismicity and shape of the subducted Nazca Plate. *Journal of Geophysical Research*, 97:17503–17529, 1992.

Cobbing, E. J., J. M. Ozard, and N. J. Snelling. Reconnaissance geochronology of the crystalline basement rocks of the Coastal Cordillera of southern Peru. *Geological Society of America Bulletin*, 88(2):241–246, 1977.

Coira, B., J. Davidson, C. Mpodozis, and V. Ramos. Tectonic and magmatic evolution of the Andes of northern Argentina and Chile. *Earth-Science Reviews*, 18(3-4):303–332, 1982.

Coney, P. J. The regional tectonic setting and possible causes of Cenozoic extension in the North American Cordillera. *Geological Society, London, Special Publications*, 28(1):177–186, 1987.

Cross, T. A. and R. H. Pilger. Constraints on absolute motion and plate interaction inferred from Cenozoic igneous activity in the western United States. *American Journal of Science*, 278(7): 865–902, 1978.

Dalmayrac, B., J. R. Lancelot, and A. Leyreloup. Two-billion-year granulites in the late Precambrian metamorphic basement along the southern Peruvian coast. *Science*, 198(4312):49–51, 1977.

DeMets, C., R. G. Gordon, D. F. Argus, and S. Stein. Current plate motions. *Geophysical Journal International*, 101(2):425–478, 1990.

Dickinson, W. R. and W. S. Snyder. Plate tectonics of the Laramide orogeny. *Geological Society of America Memoir*, 151:355–366, 1978.

Dorbath, C. Velocity structure of the Andes of central Peru from locally recorded earthquakes. *Geophysical Research Letters*, 23(2):205–208, 1996.

Dumitru, T. A., P.B. Gans, D. A. Foster, and E. L. Miller. Refrigeration of the Western Cordilleran lithosphere during Laramide shallow-angle subduction. *Geology*, 19:1145–1148, 1991.

English, J. M., S. T. S. T. Johnston, and K. Wang. Thermal modeling of the Laramide orogeny: testing the flat-slab subduction hypothesis. *Earth and Planetary Science Letters*, 214 (34):619–632, 2003.

Gutscher, M. A., H. Spakman, W.and Bijwaard, and E. R. Engdahl. Geodynamics of flat subduction; seismicity and tomographic constraints from the Andean margin. *Tectonics*, 19(5): 814–833, 2000.

Hacker, B. R. and G. A. Abers. Subduction Factory 5: Unusually low Poisson's ratios in subduction zones from elastic anisotropy of peridotite. *Journal of Geophysical Research*, 117(B6), 2012. doi: 10.1029/2012JB009187.

Hacker, B. R., G. A. Abers, and S. M. Peacock. Subduction factory 1: Theoretical mineralogy, densities, seismic wave speeds, and H_2O contents. *Journal of Geophysical Research*, 108(B1): 2029, 2003. doi: 10.1029/2001JB001127.

Hampel, A. The migration history of the Nazca Ridge along the Peruvian active margin; a re-evaluation. *Earth and Planetary Science Letters*, 203(2):665–679, 2002.

Hasegawa, A. and I. S. Sacks. Subduction of the Nazca plate beneath Peru as determined from seismic observations. *Journal of Geophysical Research*, 86(B6):4971–4980, 1981.

Havskov, J. and L. Ottemoller. SEISAN earthquake analysis software. *Seismological Research Letters*, 70(5):532–534, 1999.

Hayes, G. P., D. J. Wald, and R. L. Johnson. Slab 1.0: A three-dimensional model of global subduction zone geometries. *Journal of Geophysical Research*, 117, 2012. doi: 10.1029/2011JB008524.

Humphreys, E., E. Hessler, K. Dueker, G. L. Farmer, E. Erslev, and T. Atwater. How Laramide-age hydration of North American lithosphere by the Farallon Slab controlled subsequent activity in the Western United States. *International Geology Review*, 45(7):575–595, 2003.

James, D. E. Andean crustal and upper mantle structure. *Journal of Geophysical Research*, 76 (14):3246–3271, 1971.

James, D. E. and J. A. Snoke. Seismic evidence for continuity of the deep slab beneath central and eastern Peru. *Journal of Geophysical Research*, 95:4989–5001, 1990.

Jordan,T. E. and R. W. Allmendinger. The Sierras Pampeanas of Argentina; a modern analogue of Rocky Mountain foreland deformation. *American Journal of Science*, 286(10):737–764, 1986.

Macedo-Sánchez, O., J. Surmont, C. Kissel, and C. Laj. New temporal constraints on the rotation of the Peruvian central Andes obtained from paleomagnetism. *Geophysical Research Letters*, 19(18):1875–1878, 1992.

Mamani, M., A. Tassara, and G. Wörner. Composition and structural control of crustal domains in the central Andes. *Geochemistry Geophysics Geosystems*, 9(3), 2008. doi: 10.1029/2007GC001925.

Manea,V. C., M. Perez-Gussinye, and M. Manea. Chilean flat slab subduction controlled by overriding plate thickness and trench rollback. *Geology*, 40(1):35–38, 2011.

Menke, W. *Geophysical data analysis: discrete inverse theory*, volume 45. Academic Press, Oxford, UK, 1984.

Mitouard, P., C. Laj, T. Mourier, and C. Kissel. Paleomagnetic study of an arcuate fold belt developed on a marginal orogen: The Cajamarca deflection, northern Peru. *Earth and Planetary Science Letters*, 112(1):41–52, 1992.

Mišković, A. and U. Schaltegger. Crustal growth along a non-collisional cratonic margin: a Lu–Hf isotopic survey of the Eastern Cordilleran granitoids of Peru. *Earth and Planetary Science Letters*, 279(3):303–315, 2009.

Monger, J. W. H., R. A. Price, and D. Tempelman-Kluit. Tectonic accretion and the origin of the two major metamorphic and plutonic welts in the Canadian Cordillera. *Geology*, 10(2):70–75, 1982.

Obayashi, M., J. Yoshimitsu, and Y. Fukao. Tearing of stagnant slab. *Science*, 324(5931):1173–1175, 2009.

Ottemller, L., P. Voss, and J. Havskov. *SEISAN EARTHQUAKE ANALYSIS SOFTWARE FOR WINDOWS, SOLARIS, LINUX and MACOSX*, 2013.

Pilger, R. H. Plate reconstructions, aseismic ridges, and low-angle subduction beneath the Andes. *Geological Society of America Bulletin*, 92(7):448–456, 1981.

Ramos, V. A. The basement of the Central Andes; the Arequipa and related terranes. *Annual Review of Earth and Planetary Sciences*, 36:289–324, 2008.

Ramos, V. A. and A. Folguera. Andean flat-slab subduction through time. *Geological Society Special Publications*, 327:31–54, 2009.

Ramos, V. A., E. O. Cristallini, and D. J. Perez. The Pampean flat-slab of the Central Andes. *Journal of South American Earth Sciences*, 15(1):59–78, 2002.

Roperch, P. and G. Carlier. Paleomagnetism of Mesozoic rocks from the central Andes of southern Peru: Importance of rotations in the development of the Bolivian orocline. *Journal of Geophysical Research*, 97(B12):17233–17249, 1992.

Roperch, P., V. Carlotto, G. Ruffet, and M. Fornari. Tectonic rotations and transcurrent deformation south of the Abancay deflection in the Andes of southern Peru. *Tectonics*, 30(2), 2011. doi: 10.1029/2010TC002725.

Schneider, J. F. and I. S. Sacks. Stress in the contorted Nazca plate beneath southern Peru from local earthquakes. *Journal of Geophysical Research*, 92(B13):13887–13902, 1987.

Siebert, L. and T. Simkin. Volcanoes of the world: an illustrated catalog of holocene volcanoes and their eruptions. *Smithsonian Institution, Global Volcanism Program Digital Information Series, GVP-3*, 2002. URL `http://www.volcano.si.edu/gvp/world/`.

Somoza, R. Updated Nazca (Farallon)South America relative motions during the last 40 My: implications for mountain building in the central Andean region. *Journal of South American Earth Sciences*, 11(3):211–215, 1998.

Stevenson, D. J. and J. S. Turner. Angle of subduction. *Letters to Nature*, 270:334–336, 1977.

Tassara, A., H. J Götze, S. Schmidt, and R. Hackney. Three-dimensional density model of the Nazca plate and the Andean continental margin. *Journal of Geophysical Research*, 111(B9), 2006. doi: 10.1029/2005JB003976.

Um, J. and C. H. Thurber. A fast algorithm for two-point seismic ray tracing. *Bulletin of the Seismological Society of America*, 77(3):972–986, 1987.

van Hunen, J., A. P. van den Berg, and N. J. Vlaar. On the role of subducting oceanic plateaus in the development of shallow flat subduction. *Tectonophysics*, 352(3-4):317–333, 2002.

van Hunen, J., A. P. van den Berg, and N. J. Vlaar. Various mechanisms to induce present-day shallow flat subduction and implications for the younger Earth; a numerical parameter study. *Physics of the Earth and Planetary Interiors*, 146(1-2):179–194, 2004.

Vaughan, A. P., P. T. Leat, and R. J. Pankhurst. Terrane processes at the margins of Gondwana: Introduction. *Geological Society, London, Special Publications*, 246(1):1–21, 2005.

Wagner, L. S., S. Beck, and G. Zandt. Upper mantle structure in the south central Chilean subduction zone (30 degrees go 36 degrees S). *Journal of Geophysical Research*, 110, 2005. doi: 10.1029/2004JB003238.

Wagner, L. S., M. L. Anderson, J. M. Jackson, S. L. Beck, and G. Zandt. Seismic evidence for orthopyroxene enrichment in the continental lithosphere. *Geology*, 36(12):935–938, 2008.

Zhao, D., A. Hasegawa, and S. Horiuchi. Tomographic imaging of P and S wave velocity structure beneath northeastern Japan. *Journal of Geophysical Research*, 97:19909–19928, 1992.